MARKOV-CHAIN MONTE CARLO RECONSTRUCTION OF EMISSION MEASURE DISTRIBUTIONS: APPLICATION TO SOLAR EXTREME-ULTRAVIOLET SPECTRA

VINAY KASHYAP[1] AND JEREMY J. DRAKE[2]

Harvard-Smithsonian Center for Astrophysics, 60 Garden Street, Cambridge, MA 02138

ABSTRACT

We have developed a new method for the reconstruction of differential emission measure distributions based on a Metropolis Markov-chain Monte Carlo (MCMC[M]) method. This technique allows us to (1) relax nonphysical smoothness constraints generally imposed on DEMs, (2) determine confidence bounds on the computed values, and (3) include extra information in the form of upper limits. Using the MCMC[M] algorithm, we reanalyze extreme ultraviolet spectral line fluxes obtained from Solar Extreme Ultraviolet Rocket Telescope and Spectrograph observations by Brosius et al. to obtain differential emission measure (DEM) distributions for active and quiet regions on the Sun. Both active- and quiet-region DEMs show a probable minimum near $\log T \approx 5.6$; the quiet-region DEM drops off beyond $\log T = 6.4$, while the active-region DEM does not show evidence of a significant downturn even at $\log T = 7$. The most striking aspect of our results is that the latter also shows several sharp peaks (of width ~ 0.1 dex), notably at $\log T = 6$ and 6.3, and a broad feature, beyond $\log T = 6.5$. We also explore the limitations on DEM reconstruction imposed by imperfect atomic data, choice of spectral lines, uncertainties in abundances, and other systematic errors. Within these limitations, we discuss the derived emission measure distribution and comment on its implications to coronal structure. We conclude that calculation of uncertainties on the DEM are crucial in the interpretation of structure seen in reconstructions. Further, a careful selection of the spectral lines used to infer the DEM is needed in order to avoid "artificially" generating structure in the DEM.

Subject headings: atomic processes — radiative transfer — Sun: corona — Sun: UV radiation

1. INTRODUCTION

Surveys of the sky at UV and X-ray wavelengths have revealed the ubiquitous presence of solar-like transition regions and coronal plasma in the outer atmospheres of late-type dwarfs from spectral types mid-F to late M, and in late-type giants down to mid-K (see, e.g., Rosner, Golub, & Vaiana 1985; Jordan & Linsky 1987). One of the outstanding problems in astrophysics is the question of how this plasma is heated to temperatures of up to several tens of millions of kelvins.

The relatively low densities of the plasma in the solar outer atmosphere (e.g., $N_e \sim 10^9$–10^{10} cm^{-3} in nonflaring plasma of the solar corona) render the emission essentially optically thin and collision dominated. Although some evidence is emerging based on *Extreme Ultraviolet Explorer* (*EUVE*) spectra that some stellar coronae might reach densities as high as $N_e \sim 10^{13}$ cm^{-3} (see, e.g., the review by Drake 1996) and some authors claim resonance scattering plays a role in some coronal line spectra (Schrijveret et al. 1995; see also the counterarguments by Schmitt et al. 1996; Drake, Laming, & Widing 1997), it is reasonable to assume that stellar coronal emission is also well described as being optically thin.

Optically thin, collisionally dominated plasmas in equilibrium can be parameterized in one dimension in terms of temperature by their so-called emission measure (EM) distributions, or its differential form with respect to temperature (DEM; see § 2 for the mathematical formalism). The DEM allows for a very convenient and potentially powerful characterization of the temperature structure of the atmosphere.

The convenience lies in the relative simplicity of the one-dimensional function as compared to the complexity of observed spectra: it enables one to predict the spectrum in different bandpasses, to easily compare and combine observations of the same plasma made by different instruments in different bandpasses, and in principle to perform quantitative comparative studies of different observations of different plasma sources. In short, the DEM represents a simple source model that might be applied as long as the underlying assumptions in the optically thin, collisionally dominated radiative-loss model are applicable (see § 3).

The thermodynamic state of the plasma source itself is determined by its response to sources and sinks of energy, as governed by the straightforward concept of energy conservation. In principle, if the thermodynamic state of the atmosphere can be inferred through observation and derivation of the DEM, and if we can understand all the sinks of energy that are significant, then the form of the heating function can be diagnosed through application of the equations of energy balance (see, e.g., Jordan 1980, 1992, and references therein). In practice, there are likely to be manifold complexities in the actual energy balance caused by effects such as mass flows, diffusion, and highly complicated topology, rendering this process somewhat difficult at best. A detailed discussion of this problem in the solar context is presented by Mariska (1992). Despite the likely intractability of this inverse problem (DEM techniques have been used for 30 years, yet the coronal heating problem has not been solved), the DEM still provides convenient observational constraints on heating theories: successful theories must be able to account for the range of observed DEMs,

[1] kashyap@head-cfa.harvard.edu.
[2] jdrake@head-cfa.harvard.edu.

both in the solar outer atmosphere and in stars of different spectral types and activity levels.

Extracting the actual source DEM from observed quantities (usually spectral line fluxes), while conceptually simple, is actually an ill-conditioned problem with no truly unique solution unless additional constraints are imposed. Consequently, a number of different methods of attack have been devised to tackle the problem, and a commensurate amount of critique has been written about these. In particular, we draw attention to Craig & Brown (1976) and to the very recent work of Judge, Hubeny, & Brown (1997), who present detailed analyses of the difficulties in the inversion problem from an analytical point of view. We discuss some of the main issues in brief in the following section.

Despite the potential drawbacks, the DEM inference problem is of growing topical interest because of the rapidly expanding database of EUV and X-ray spectroscopic observations of stellar coronae, as realized for the case of the Sun by, e.g., the *Solar and Heliospheric Observatory* (*SOHO*) and the Solar EUV Rocket Telescope and Spectrograph (SERTS) and in the stellar case by, e.g., the *Extreme Ultraviolet Explorer* (*EUVE*) and (at lower spectral resolution) the *Advanced Satellite for Cosmology and Astrophysics* (*ASCA*). While several different DEM inversion methods have been applied to data obtained from these missions, many of these do not offer the ability to investigate the significance of the resulting DEM structure, or else, to aid the inversion process, they impose mathematical constraints that have no physical basis, such as smooth derivatives, or that are not rigorously repeatable for disparate data sets, such as fits based on polynomials. Such methods render it extremely difficult to compare DEMs derived from different sets of observations. Moreover, inversion methods that do not provide some estimate of the uncertainty in the EM at each temperature are of little use for comparative studies of coronal structure in different types of stars, or indeed, of changes in coronal structure in different observations of the same star.

In this paper, we apply a new method of DEM reconstruction to solar EUV data and discuss the problems inherent in the process of deriving and interpreting DEMs. Our main contentions are, first, that "unsmooth" structure in the resulting DEMs fits observed line fluxes better than "smooth solutions," but that this structure may arise solely as a result of problems with the underlying atomic data, or impropriety of the underlying assumptions of the DEM approach; and second that, without rigorous estimates of the DEM uncertainty, the derived DEMs can be of little astrophysical value or can even be misleading.

Our DEM reconstruction method employs a Markov-chain Monte Carlo (MCMC) algorithm. This approach is based on a Bayesian formalism that allows us to infer the best set of model parameters that describe the observed data even if the problem is ill constrained. The method allows straightforward generalization to any number of dimensions such that, in principal, elemental abundances and plasma densities may also be derived simultaneously with the DEM (see, however, the discussion of Judge et al. 1997 concerning the problems regarding the density inversion).

We outline the spectral line database used in our analysis in § 2 and describe the formalism of differential emission measures and problems associated with deriving them in § 3. We then describe our analysis and filtering of the data

in § 4. The MCMC-based algorithm and its implementation are detailed in § 5.1.2, and verification of the technique with simulated data is discussed in an Appendix. The results are discussed in § 6 and summarized in § 7.

2. OBSERVATIONS: SOLAR EUV LINE INTENSITIES

A solar active region (NOAA AR 7563) and quiet-Sun regions were observed during a flight of the Solar EUV Rocket Telescope and Spectrograph (Neupert et al. 1981; Thomas & Neupert 1994; Brosius et al. 1996) in the 280–420 Å region (1993 August 17; cf. Brosius et al. 1996; hereafter B96); subsequent detailed analysis by B96 (who also present similar analyses of SERTS spectra obtained in earlier flights) resulted in the detection and identification of 65 lines in the active-region (hereafter AR93) spectrum and 57 lines in the quiet Sun (hereafter QS93) spectrum. B96 describe the data reduction and the measurement of fluxes for these sets of spectral lines. We adopt their line fluxes here.

B96 derived DEMs using the cubic spline method of Monsignori-Fossi & Landini (1991), applied to a subset of the data—spectral lines forming pairs whose line ratios are temperature and density insensitive (we have not followed this procedure; see § 4.2.3). Two of our aims are to use the spectral line intensities of B96 in order to test our DEM reconstruction method and to examine the nature of the resulting DEM distributions. We therefore note that, while the atomic data used by B96 to interpret observed line intensities is often in common with that used by us in this study (see below), there are some differences that prevent an entirely direct comparison of our results with those of B96.

3. DIFFERENTIAL EMISSION MEASURES

3.1. *Formalism*

The formalism of the DEM analysis was first developed by Pottasch (1963), and later by Jeffries, Orral, & Zirker (1972), Withbroe (1975), Jordan (1976) and Craig & Brown (1976); a detailed treatment for the solar context can be found in Bruner & McWhirter (1988). For the purposes of clarity in the material presented elsewhere in this paper, we describe here the fundamental assumptions and equations pertinent to the DEM reconstruction process here.

The DEM method is based on the following assumptions with regard to the state of the emitting source:

1. Optical depths within the source are negligible.
2. Collisions dominate excitation and ionization processes.
3. Excitation and ionization processes are in statistical equilibrium.
4. Electrons and ions have Maxwellian velocity distributions characterized by the same temperature.
5. The elemental composition does not vary within the corona.

The lack of significant optical depth in a collision-dominated plasma means that any one volume element of plasma is radiatively decoupled from any other volume element; the plasma can then be thought of simply as a collection of quasi-isothermal plasmas of different temperatures, each occupying a different volume element. The emergent intensity of a given spectral line from one of these isothermal plasma elements simply depends on the volume integrated product of the number density of the emitting

ionic species, the number density of the line-exciting species (mostly electrons) and the appropriate excitation coefficient describing the efficiency of the line excitation mechanism. For a given transition, this product is proportional (through the ionization state of the plasma and the relative abundance of the element in question) to N_e^2, where N_e is the electron number density. For a transition $u \to l$, the line intensity

$$I_{ul} = K_{ul} \int_{\Delta T_{ul}} A G_{ul}(T, N_e) N_e^2(T) dV(T) , \qquad (1)$$

where K_{ul} is a known constant, which includes the wavelength of the transition and the stellar distance, A is the elemental abundance, and $G_{ul}(T, N_e)$ is the "contribution" function of the line containing all the relevant atomic physics parameters. In the solar context, the above integral is often carried out over the plasma depth rather than the volume. Note that G_{ul} is only a weak function of N_e; density-sensitive spectral lines may be used to constrain the values of N_e prior to DEM analysis, so we will henceforth write $G_{ul} = G_{ul}(T)$. The quantity $N_e^2(T)V(T)$ is usually referred to as the "volume emission measure" (VEM). Recasting this integral into one over the temperature, T, of the emitting plasma, we then form the expression for the total intensity of a spectral line:

$$I_{ul} = A K_{ul} \int_{\Delta T_{ul}} G_{ul}(T) \overline{N_e^2(T)} \frac{dV(T)}{d \log T} d \log T , \qquad (2)$$

which would in the cgs system have the units ergs cm^{-2} s^{-1} sr^{-1}. Here, we have used the last two of the assumptions enumerated above, and the VEM has been transformed to its logarithmic differential form the differential emission measure

$$\mathrm{DEM}(T) = N_e^2(T) \frac{dV(T)}{d \log T} . \qquad (3)$$

Craig & Brown (1976) provided the first rigorous definition of the DEM as a weighting function, or source term, in the integral equation for the line intensity that one is attempting to solve.

3.2. Sources of Uncertainty

In practical application, it is important to realize that all the terms in equation (2) are subject to errors and uncertainties. Not only are these present in the directly observed quantities (the line fluxes I_{ul} and scale factors K_{ul}), but also in the atomic data and ion populations (represented by $G_{ul}(T)$; see § 3.2.3) and abundances A (see § 4.2.2), and even in the coarseness of the integration represented by $d \log T$ (see § 3.3). Blends of additional unresolved lines not considered in line flux measurements (§ 3.2.1) and errors in instrument calibration (§ 3.2.2) also contribute to systematic errors in the measured fluxes. In addition, the underlying assumptions in equation (2) may be invalid (cf. Lang, Mason, & McWhirter 1990). The uncertainties in the element abundance and in the scale factor K_{ul} are the same for lines of the same element and can be dealt with trivially. In this work, we avoid the problem of coarse gridding by using a temperature grid that oversamples the contribution functions (and defer a discussion of variable bin sizes and its consequences to future work).

3.2.1. Line Blending

Even at the resolution of the SERTS instrument, line blending can sometimes be a problem. Line blends and line misidentifications can be diagnosed to some extent through comparisons of the EMs predicted by different lines of the same ion, as illustrated by the recent paper by Young et al. (1998; hereafter Y98). In § 4.2.3, we discuss the lines we discard from our DEM reconstructions because of suspected blending.

3.2.2. Instrument Calibration

Probable instrument calibration problems concerning the SERTS 1989 flight were uncovered by Y98, who were lead to suggest a modification in the calibration corresponding to a lowering of the effective area longward of 400 Å. B96 touched upon the calibration of the SERTS 1993 spectra and verified quantitatively using density- and temperature-insensitive line ratios that there appears to be no large systematic problems as functions of wavelength. Absolute calibration is not important for our DEM reconstruction since this simply represents a global normalization factor for the DEM as a whole. Issues such as that unearthed by Y98 are a potential problem, however. In our DEM reconstructions described below, we do note an unexpectedly larger scatter in a comparison between a subset (data set [a] of § 4.2.3) of observed line fluxes and those predicted using the reconstructed DEM near 350 Å, which could possibly be related to residual calibration uncertainties at this wavelength.

3.2.3. Line Contribution Function

Proper treatment of the systematic uncertainties in $G_{ul}(T)$ is nontrivial, partly because of its complex nature (see also the discussion by Lang et al. 1990; Judge et al. 1997), but also because it lies inside the integral over temperature. Because of the difficulties involved, rigorous inclusion of realistic uncertainties in $G_{ul}(T)$ has never been done in any studies involving construction of DEMs from observed line intensities. Instead, here we apply the practical, but almost certainly inadequate, approximation that the uncertainty $\delta G_{ul}(T)$ for any given transition is independent of temperature, $\delta G_{ul}(T) \to \delta G_{ul}$. We can then incorporate coarse estimates for the uncertainties in G_{ul} in the final DEM through simple quadrature addition with the other sources of uncertainty.

The two dominant sources of uncertainty for a given spectral line are the collisional excitation rate and the ion population. Uncertainties in the atomic physics in analyses such as those presented here (i.e., based on spectral lines from different elements at different ionization stages) are very difficult to assess rigorously. This is because many of the uncertainties can be correlated in complicated ways and, moreover, change with temperature; the assumed ionization balance is an obvious case for which all lines of a given ion share the same uncertainty. Unfortunately, for many lines observed in reasonable quality spectra, especially those involving more complicated terms, the errors in the atomic physics parameters are likely to dominate the observational errors. For example, Drake, Laming, & Widing (1995) assessed a nominal 30% error on predicted strengths of lines observed in *EUVE* spectra based on critically compiled and assessed, and on specially recalculated, atomic data. While probably realistic for the more simple transitions for which recent theoretical work exists, this

nominal uncertainty will be overly optimistic in the case of more complex ions and transitions. Some discussion illustrating the sometimes large and problematic differences in the predicted line spectra of the widely available optically thin plasma radiative-loss models, such as those of Monsignori-Fossi & Landini (1994) and Kaastra, Mewe, & Nieuwenhuijzen (1996b), can be found in Brickhouse et al. (1995), and references therein.

The different ion balance calculations, such as those for Fe by Arnaud & Raymond (1992) and Arnaud & Rothenflug (1986), lead to differences in the profiles of the contribution functions $G_{ul}(T)$, thus changing the predicted line emissivities themselves and causing the peak contribution temperatures of spectral lines to shift. This latter effect may be as large as 25%; e.g., the shift in Fe XVII between the calculations of Arnaud & Rothenflug (1986; 4×10^6 K) and Arnaud & Raymond (1992; 5×10^6 K). In addition, the available calculations generally correspond to the low-density limit ($\lesssim 10^8$ cm^{-3}) and of necessity ignore more complicated case-specific nonequilibrium effects that may arise, e.g., in siphon flows in coronal loops (Spadaro et al. 1995).

We also note that, while the ion balance calculations of Arnaud & Raymond (1992) include more realistic treatments of the relevant physical processes than those of Arnaud & Rothenflug (1986), they are available only for Fe, and the latter do provide a more consistent set of calculations for considering together lines due to different elements. Indeed Laming, Drake, & Widing (1995) preferred the earlier work in their study of solar coronal element abundances for this reason.

We discuss further the effects of the sources of the errors touched upon here on our DEM reconstructions in § 6.1 below. Further analytical discussion of the problems of systematic errors in DEM reconstruction can be found in Judge et al. (1997).

3.3. *Implicit Difficulties in Reconstructing the DEM*

The DEM(T) is observationally derived through inversion of equation (2) based on measurements of spectral lines formed at different temperatures. The inversion of this type of equation (Fredholm equation of the first type) poses well-known mathematical difficulties. Earlier discussions and treatments of this problem have been presented by several different authors (see, e.g., Jeffries et al. 1972; Withbroe 1975; Sylwester et al. 1980; Craig & Brown 1986; Siarkowski 1983; the collection of papers in Harrison & Thompson 1991; and more recently, Mewe et al. 1995; and Judge et al. 1997, to name a few).

From equation (2), it can be seen that the temperature range over which information can be provided on the DEM by any one spectral line depends critically on the "contribution function" $G_{ul}(T)$. In order to derive the DEM over a wide range of temperature, a number of different spectral lines, or indices, with different $G(T)$ functions must be observed. If a large number of spectroscopically accessible indices covering a large range in temperature but each formed over only narrow and mutually exclusive ranges of temperature are available, the inversion of equation (2) is well-constrained. However, spectral lines are formed over quite large ranges in temperature determined primarily by the parent ion population [the $G(T)$ functions have typical widths of $\Delta \log T \sim 0.3$]. The most problematic aspect of the inversion problem then lies in the dependence of the solution at any one temperature on the solution at other temperatures because the spectral lines used to diagnose the EM distribution are formed over this finite range in temperature. The problem is akin to that of reconstructing an image based on scanning only the integrated intensity through a window of finite size at only a limited number of locations. In our case, we are using each spectral line as a windowing function on the underlying emission measure distribution. This concept is important because it means that the resolution and extent of our best possible reconstruction of the actual EM distribution is entirely dependent on the available window functions—in our case, the available spectral lines.

Craig & Brown (1976) presented the first detailed mathematical analysis of the problems of DEM inversion for the specific case of stellar EUV and X-ray spectra. They argued, perhaps somewhat pessimistically, that spectral line contribution functions—the $G(T)$ functions—do not provide adequate temperature resolution to define the DEM with any astrophysically useful precision. The problem they highlighted in detail is one inherent in the integral equation (2): solutions with components of higher frequency than the $G(T)$ functions are not constrained, and so for any given set of spectral lines, there are an infinite number of solutions for $N_e^2 \, dV(T)/\log T$ that satisfy it. This viewpoint was criticized by Sylwester, Schrijver, & Mewe (1980), who argued that enforcing positivity in the DEM provides an additional powerful constraint that is grounded in the physics of the problem (see also Schmitt et al. 1996). However, even with the positivity constraint, "useful" solutions to the inversion must include additional constraints in order to restrict the range of possible solutions. These additional constraints involve artificial smoothness criteria.

Smoothness criteria are introduced either in an explicit fashion, such as the smoothed second derivatives of Mewe et al. (1995) and the "adaptive smoothing" technique of Thompson (1991), or implicitly, as in the cubic spline interpolation method of Monsignori-Fossi & Landini (1991), the polynomial fitting method of Dammasch (1991), or the Chebychev polynomial method of Stern et al. (1995), or even simply through the choice of the discretization size of the temperature grid. The main astrophysical drawback of these smoothing techniques is that they are not motivated by physical considerations of the source or the observing instrument and so might discriminate against situations in which the actual DEM is not particularly smooth. For example, Schmitt et al. (1996) have pointed out that models of coronal loops do not have smooth DEMs because they are generally parameterized by maximum temperatures that define a discontinuity in their EM distributions (cf. Rosner, Tucker, & Vaiana 1978; Serio et al. 1981; Rosner et al. 1985).

In the analysis that follows, we develop a local smoothing method using the form of the contribution functions $G_{ul}(T)$ of the observed spectral lines (see § 5.2.3). Using this approach, we sidestep the problem of ill conditioning that arises if the temperature grid is significantly finer than the widths of the line contribution functions, and we also avoid the artificial smoothness and rigidity constraints such as are imposed by polynomial or spline fitting or by limits on derivatives of possible solutions. Our technique thus allows us to detect the finest structure that our observational data allow; if the source DEM contains structure on a finer scale than this, then it *cannot be detected*.

4. DATA ANALYSIS

4.1. *Atomic Data*

Throughout this work we have adopted the CHIANTI database of energy levels, collision strengths, and transition probabilities (Dere et al. 1997). This database represents the most up-to-date compilation of atomic data currently available for interpreting EUV lines produced in the optically thin, collisionally dominated regime. Y98 describe a detailed comparison of theoretical line strengths and observed line intensities from spectra obtained by SERTS during a rocket flight made in 1989. In one or two cases, more recent calculations of collision strengths than those included in CHIANTI are now available, though we have not attempted to include them here; some are discussed by Y98. We have made extensive use of the Y98 study for verifying the quality of both the atomic data in CHIANTI corresponding to the B96 lines and of the lines themselves (§ 4.2.3). We have employed the ionization equilibria of Arnaud & Rothenflug (1986) for all elements other than Fe, for which we adopt the more recent calculations of Arnaud & Raymond (1992) unless stated otherwise.

4.2. *Filtering of Observational Data*

4.2.1. *Emission Measures from Individual Ions*

The first stage in our analysis involves the construction of EM distributions for the observed line fluxes from different ions using a method similar to that of Pottasch (1964). This allows us to see immediately whether or not any of the different lines common to a particular ion show discrepancies with respect to other lines of the same ionic species or with respect to the global EM distribution. Comparing the EMs predicted by ions of different elements also allows us some leverage on ascertaining whether or not the elemental abundances adopted are appropriate. A similar approach was used recently by Laming et al. (1995) in the study of element abundances and the first ionization potential (FIP) effect in solar and stellar coronae. We discuss the issue of elemental abundances in more detail below. The method adopted here differs from that of Laming et al. (1995) in the range of integration over the individual line contribution functions $G_{ul}(T)$ (e.g., eq. [1]), which here we take to be the between the points in temperature at which $G_{ul}(T)$ has dropped to 10% of its peak value.

The EMs derived from the AR93 and QS93 line intensities reported by B96 are shown in Figure 1; each point represents the EM averaged over all lines for a given ion, while the error bars represent the scatter in the EMs predicted for individual lines of a given ion. (The measurement errors on the fluxes [and hence the EMs] are generally $\sim 10\%$; these are not shown on the plots for purposes of clarity and because of potential systematic offsets; see below.) Each element is represented by a different symbol type, and low-FIP and high-FIP elements can be distinguished by open and filled symbols, respectively. For the purposes of these plots, we have used the "coronal" elemental abundances of Feldman et al. (1992); the abundances were also used in the B96 study. They include a systematic enhancement of low-FIP elements relative to high-FIP elements by an average factor of ~ 4 relative to, for example, the photospheric abundances compiled by Grevesse, Noels, & Sauval (1992) (see also § 4.2.2). Also shown for purposes of comparison are the DEM reconstructions of B96 (taken from their Figs. 8a and 9a). We first
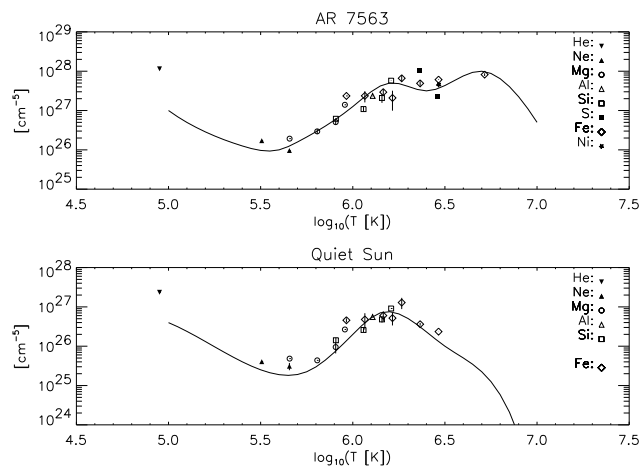

FIG. 1.—Emission measures (EM) (in cm^{-5}) derived from combining all lines for particular ions, for the active (*upper panel*) and quiet-Sun (*lower panel*) regions observed by SERTS. 1 σ error bars have been shown when multiple lines from the same ion have been combined to produce a single ion-averaged EM. The measurement error on each line is approximately 10% and is not shown for reasons of clarity. Each symbol refers to an ion of a particular element, as listed to the right; see Table 2 to determine the ionic states. Following Brosius et al. (1996), we have assumed the solar coronal abundances of Feldman et al. (1992) for the purposes of these plots. The DEMs (in cm^{-5}) derived by Brosius et al. are represented by the solid curves. Note the quite large scatter in the EMs predicted by individual lines of some ions, as represented by the error bars (e.g., Fe XIII).

discard the point due to He II $\lambda 303.8$ from this discussion and that following since it is likely to have significant optical depth and contributions from radiative recombination. Having done this, one sees immediately that there is excellent general agreement between the distribution of EM points and the B96 reconstructions; however, there is also significant scatter and some disagreement between different ions in the former.

We note that a systematic offset between our EM points and the B96 curves can result from our "Pottasch"-type of approximation that the line emission arises from a limited temperature range, centered at the peak in the line contribution function, and that the EM is assumed constant within this range. If the EM points are rederived taking into account the slope in the EM distribution, they move in both temperature and magnitude and generally in the direction along the slope toward higher EM, depending somewhat on the exact nature of the EM curve and on the individual line contribution functions (cf. the study of ϵ Eri by Laming, Drake, & Widing 1996). Additional scatter in the EM points, and the error bars in the EM points themselves, can arise from several different sources of systematic errors as well as the random errors of measurement. As discussed earlier in § 3.2, the largest source of scatter is likely to be errors in the atomic data.

The scatter in the EMs in Figure 1 calculated simply from the B96 observed intensities demonstrate that "blind" EM reconstruction and interpretation, even of quite high quality spectral data such as that collected by SERTS, could be perilous without detailed consideration of these underlying uncertainties. The true uncertainty in an EM distribution reconstructed from the whole set of lines used in Figure 1 without further refinements is reasonably represented by the scatter in the points in regions where the points are dense. At temperatures with relatively few points, and for

different EM distributions with much steeper gradients or more complicated structures, the uncertainty in the EM cannot be readily estimated for reasons discussed in § 3. Clearly, any quantitative comparison of different EM distributions requires an estimate of the uncertainties in the EM reconstructions. These uncertainties can be calculated properly only through consideration of the various sources of error propagated through the EM reconstruction process.

4.2.2. *Element Abundances*

Following the confirmation by Meyer (1985) and others (see, e.g., the review by Feldman 1992) of earlier suspicions that the solar coronal composition differed from that of the photosphere, the subject of element abundances in solar (and stellar) coronae has been rapidly expanding. In the solar corona, there appears to be an abundance anomaly related primarily to the element FIP, with low-FIP elements being enhanced with respect to the photospheric mixture to varying degrees but by average factors of 4 or so relative to high-FIP elements (Feldman 1992).

From the standpoint of EM reconstruction, lack of knowledge of the underlying composition represents an additional systematic error when considering lines from different elements. For lines of the same element, it represents an uncertain normalization factor for the EM (e.g., eq. [2]) and so does not affect the derived DEM structure.

The B96 lines do not contain a sufficient number of high-FIP lines to investigate in detail the presence or not of a FIP Effect. We note that an earlier EM study (J. M. Laming 1998, private communication) of the SERTS 1989 observations of an active region yielded abundances of low- and high-FIP elements consistent with the "average" coronal abundances of Feldman et al. (1992). In the B96 data, the only high-FIP lines throughout most of the corona (i.e., at log $T > 6$) are those of S XII and S XIV from the AR93 spectrum; however, from Figure 1 we see that toward log $T \sim 5.5$ we become reliant on lines of Ne, a high-FIP element (we ignore He II), in both AR93 and QS93 data sets.

The ion balance calculations of Arnaud & Rothenflug (1986) show the populations of Ne VI and Mg VI ions to have very similar temperature dependences, and consequently the contribution functions for lines of these ions are also similar. This has lead to many interesting works based on comparisons of relative Ne VI and Mg VI line strengths, whose ratios can then yield directly the relative Ne and Mg abundances (see, e.g., Sheeley 1996, and references therein). Our Ne VI and Mg VI EM points at log $T = 5.65$ in Figure 1 are clearly more consistent with the "average" solar coronal composition of Feldman et al. (1992) than with the photospheric composition of Grevesse et al. (1992). Had we adopted the latter abundances for this figure, the Mg VI point would have been placed a factor of 4 or so higher and the two points would have been separated by a factor of 6 or more.

The situation toward higher temperatures in the active region is less clear. Of the S XII and S XIV points, the latter is more indicative of a low-FIP enhanced coronal composition. However, later on we exclude this line from our DEM inversion (see below) because of potential problems with either the atomic data or instrument calibration, as was also mentioned by Y98. The S XII point in Figure 1 is consistent with the general trend of EM with temperature for the assumed coronal composition. However, it lies considerably

above the points corresponding to Fe XIV, XV and XVI and is more consistent with a photospheric composition.

We find no evidence for a specially high Al abundance based on the EM predicted by Al X λ332.8 when compared to the other low-FIP points, as was found by J. M. Laming (1997, private communication) for earlier SERTS spectra obtained in 1989, and by Falconer, Davila, & Thomas (1997) for spectra obtained in 1991. Al has a FIP of 6 eV, which is lower than those of Mg, Si, and Fe. Feldman (1992) has discussed the possible additional compositional fractionation of the very low-FIP elements with respect to elements such as Fe. Such a fractionation is potentially very valuable for understanding coronal abundances since it points to more specific fractionation sites than the simple high-/low-FIP fractionation: it suggests that such a site should be characterized by a substantial difference between the fractions of the "high" low-FIP elements and "low" low FIP in neutral and ionized states.

In what follows, since we have rather few high-FIP points, we adopt the photospheric abundances of Grevesse et al. (1992) as our baseline composition, but we investigate the effects of assuming the Feldman et al. (1992) coronal composition on our DEM inversions.

4.2.3. *Final Choice of Lines*

Avoiding spectral lines for which there are known or suspected problems in either the atomic data, instrument calibration, or other aspects is a fundamental aspect of spectroscopic analysis in all wavelength regimes. We have been careful in constructing a subset of the initial B96 line lists that does not include lines with known or suspected discrepancies. The lines that have been excluded are listed below, together with notable lines that have been retained.

He II: We exclude λ304 from the DEM analysis because of likely complications in its formation resulting from radiative recombination and radiative transfer.

Mg VI: The only line of Mg VI from those in the SERTS bandpass in the B96 data is λ349.16. Y98 point out problems in the λ349.16/λ400.67 intensity ratio in the SERTS 1989 data, suggesting that λ349.16 could be too strong. We *retain* it here since it is a useful comparison line for Ne VI and the lowest temperature low-FIP line in the B96 data.

Mg VII: We exclude λ319 because it is blended with Ni XV (see B96; Y98).

Mg VIII: We exclude λ312 because of blending with Ni XV (see B96; Y98).

Si XI: We retain λ303 despite its proximity to He II λ304 since they seem well resolved in the SERTS spectrum; however, we exclude λ365.4 (which appears only in AR93) because of potential blending with nearby lines from Fe X, Ne V, and Mg VII.

S XIV: We exclude λ417.64 since Y98 found that the ratio λ417.64/λ445.66 disagreed with theory in the SERTS spectrum obtained in 1989 (Thomas & Neupert 1994); the disagreement could be as much as 30%. This line is toward the end of the SERTS wavelength scale and is also possibly prone to calibration uncertainties.

Fe X: We exclude λ365.5, which is present in only the QS93 list, because of a likely blend of Ne V. Y98 report a discrepant observed branching ratio with λ345.74 in the SERTS 1989 data and attribute this to Ne V λ365.60.

Fe XI: λ358.69 is likely a blend of up to four lines according to Y98, and indeed in the B96 data set this line yields an EM that is too high compared with the other Fe XI lines.

The other blends are Si XI $\lambda 358.65$, Ne VI $\lambda 358.69$, and an Fe XIV line suggested by Bhatia et al. (1994). We exclude $\lambda 358.69$. Y98 also suspected blending in $\lambda 308.58$ based on the rather high density indicated by the $\lambda 308.58/\lambda 352.67$ ratio. We estimate the density from the B96 line intensities to be log $Ne = 9.6$ or so, which is consistent with results from other diagnostics (cf. B96), and *retain* this line.

Fe XII: Y98 found problems with the $\lambda 382.85/\lambda 338.27$ branching ratio, attributing the likelihood of blending in $\lambda 338.27$ as the probable culprit. We exclude this line. Similarly, we exclude $\lambda 364.50$ because of blending with Si XI $\lambda 364.50$, though the contribution of the latter to the feature is likely to be small according to the estimate of Y98.

Fe XIII: Individual Fe XIII lines show considerable density sensitivity, and in addition the observed density-insensitive line ratios are inconsistent with theoretical predictions (see, e.g., Y98). These lines are included in the analysis of B96, but are all excluded here except for $\lambda 348.2$. This line is excited principally from the ground level, and density effects should not be a problem. P. R. Young (1997, private communication) has noted that the density-insensitive ratio $\lambda 312.17/(\lambda 348.20 + \lambda 359.67)$ does not agree with theory, and the $\lambda 359.85/\lambda 348.2$ branching ratio is also slightly discrepant, suggesting either a blend in $\lambda 348.2$ or else problems with the theoretical ratios.

Fe XV: Y98 note that $\lambda 312.57$ is blended with Co XVII; although Y98 estimate the contribution from Co based on the observed strength of Co XVII $\lambda 339.54$ to be relatively small ($\sim 15\%$), we discount this line because of this uncertainty. From the SERTS 1989 observations, Y98 derive a branching ratio for $\lambda 312.54/\lambda 327.03$ that differs from the theoretical ratio by 25%. We neglect $\lambda 417.25$ because of similar discrepancies in the $\lambda 417.25/284.16$ ratio, relying instead on $\lambda 327.03$ and $\lambda 284.16$, whose ratios are in good agreement both here and in the SERTS 1989 observations.

Undetected Lines: In Table 1 we list lines *not* detected by

SERTS and that are potentially useful for constraining the DEM toward higher temperatures. We also list the fluxes predicted at $T = 10^7$ K by an EM $= 10^{28}$ cm^{-5} for these lines for comparison purposes; they are all expected to lie well below the SERTS detection limit. (We assume a detection limit of ~ 9 and ~ 2.5 ergs s^{-1} cm^{-2} sr^{-1} for the AR93 and QS93 spectra, respectively, based on the marginal detections of Fe XVII $\lambda 347.8$ in AR93 and Fe XI $\lambda 356.6$ in QS93 spectra.) We use these lines as censored data points in our data set [c].

The undetected lines allow us to explore the DEM over a wider temperature range—clearly, the lack of lines formed at high temperatures place an upper bound on the high-temperature DEM. The temperature coverage of the detected lines is illustrated in Table 2, which lists the temperatures of peak contribution of the different ions, averaged over the B96 lines for each ion.[3]

[3] This temperature does differ for individual lines (the values quoted in Table 2 are the result of averages over $G_{ul}(T)$ for the different lines), but because its value is dominated by the ion balance, the differences are at most ~ 0.1 dex, and hence are ignored here.

TABLE 1
UNDETECTED LINES

Line	$\log_{10} (T_{max})$[a] (K)	Predicted Flux[b] (ergs s^{-1} cm^{-2})
Fe XXIV $\lambda 292$......	7.1	30
Fe XXI $\lambda 336$	7.0	25
Fe XX $\lambda 384$	6.9	50
Fe XVIII $\lambda 362$......	6.85	10

[a] Ion balance from Arnaud & Raymond 1992.
[b] Corresponding to log $T = 7.0$, log EM $= 28.0$.

TABLE 2
ATOMIC DATA REFERENCES AND TEMPERATURES OF MAXIMUM CONTRIBUTION OF RELEVANT IONS

Ion	$\log_{10} (T_{max})$[a] (K)	References[b]
He II	4.95	Aggarwal et al. 1991, 1992; Unnikrishnan, Callaway, & Oza 1991
Ne V	5.50	Aggarwal 1984; Bhatia & Doschek 1993; Burke & Lennon 1994
Ne VI	5.65	Zhang, Graziani, & Pradhan 1994; D. H. Sampson & H. L. Zhang 1995, private communication
Mg VI	5.65	Bhatia & Mason 1980
Mg VII	5.80	Bhatia & Doschek 1995
Mg VIII	5.90	Zhang et al. 1994; D. H. Sampson & H. L. Zhang 1995, private communication
Mg IX	5.95	Sampson, Goett, & Clarke 1984; Zhang & Sampson 1992
Al X..........	6.10	Zhang & Sampson 1992
Si VIII	5.90	Bhatia & Mason 1980
Si IX	6.05	Bhatia & Doschek 1993
Si X	6.15	Zhang et al. 1994
Si XI	6.20	Sampson et al. 1984; Zhang & Sampson 1992
S XII	6.35	Zhang et al. 1994
S XIV	6.45	Zhang, Sampson, & Fontes 1990
Fe X	5.95 (6.05)[c]	Pelan & Berrington 1995; Berrington & Pelan 1995
Fe XI	6.05 (6.10)[c]	A. K. Bhatia & G. A. Doschek 1996, private communication
Fe XII........	6.15	Flower 1977; Tayal, Henry, & Pradhan 1987
Fe XIII	6.20	Fawcett & Mason 1989
Fe XIV	6.25	Dufton & Kingston 1991; Storey, Mason, & Saraph 1996
Fe XV........	6.35 (6.30)[c]	A. K. Bhatia, H. E. Mason, & C. Blancard 1995, private communication
Fe XVI	6.45 (6.35)[c]	Sampson, Zhang, & Fontes 1990
Fe XVII	6.70 (6.60)[c]	Bhatia & Doschek 1992
Ni XVIII......	6.45	Sampson et al. 1990

[a] Ion balance from Arnaud & Raymond 1992.
[b] Collision strength data used in CHIANTI (Dere et al. 1997).
[c] Ion balance from Arnaud & Rothenflug 1986.

5. DEM RECONSTRUCTION ALGORITHM

Here we describe the algorithm we have developed to estimate the DEM that gives rise to the observed line fluxes. The algorithm is based on a Markov-chain Monte Carlo process (see, e.g., the review by Neal 1993)[4] that can effectively deal with both the large number of parameters (set by the number of temperature bins defining the DEM [>10, <100] and the abundances of the elements under consideration) as well as censored data (upper limits to line fluxes).

5.1. Method

5.1.1. Bayesian Analysis

The general thrust of our algorithm is to obtain the most probable set of model parameters that describe the data. We infer these probabilities by adopting a Bayesian approach (see, e.g., Loredo 1990; Gregory & Loredo 1992, 1996; Piña & Puetter 1993; Tolstoy & Saha 1996): we evaluate the probability of a specified set of N model parameters $\Theta = \{\theta_v, v = 1 \ldots n\}$ given the set of m data points $D = \{D_i, i = 1 \ldots m\}$ using Bayes' Theorem,

$$p(\Theta \mid D) = p(\Theta) \frac{\prod_{i=1,m} p(D_i \mid \Theta)}{p(D)} , \qquad (4)$$

where $p(\Theta)$ is the a priori joint probability[5] of the model parameters (which are assumed to be independent of each other), $p(D_i \mid \Theta)$ is the likelihood of observing the given datum D_i for the specified set of model parameters, and $p(D)$ is a normalization factor that ensures that the computed probability is normalized to unity (this is a matter of convenience, and enables us to identify a probability of 0 with impossibility and 1 with certainty). Determination of the so-called "posterior probability distribution" $p(\Theta \mid D)$, which forms a joint distribution in n dimensions, constitutes a complete solution to the general inference problem for the specified model (a model here refers to the adopted set of the parameters Θ, not to any particular set of values of the parameters themselves). Probability distributions of a single parameter (θ_μ, say) may be determined by computing the effects of varying all the other parameters while holding the relevant parameter fixed—in other words, by marginalizing the joint distribution over these nuisance parameters (so-called because they are not relevant to the particular problem being considered),

$$p(\theta_\mu \mid D) = \int p(\Theta \mid D) \prod_{v \neq \mu} d\theta_v ,$$

and may then be summarized either by the mode [value of θ_μ where $p(\theta_\mu \mid D)$ is maximum] or by the mean [$\langle \theta_\mu \rangle = \int \theta_\mu p(\theta_\mu \mid D) d\theta_\mu$]. Note that in many cases $p(\theta_\mu \mid D)$ may be asymmetrical and would require a more complex summari-

---

[4] The review by Neal (1993) is available on-line at http://www.cs.toronto.edu/—radford/review.abstract.html.
[5] As the name suggests, these are the probabilities one assigns to the parameter values *before* the calculation begins and contain the sum total of our knowledge about these parameters up to that point. If nothing is known of them save a range of valid values, then a uniform probability density is adopted. If the value of the parameter is known exactly, then a δ-function prior is adopted. The concept of prior probability functions has generally caused much controversy (see, e.g., Loredo 1990), but it must be noted that the only times they affect the posterior probability function is when a significant amount of information is known about the parameters. As such they are extremely useful in updating information about the model parameters.

zation: e.g., a *credible region* (or confidence interval) may be set on θ_μ by requiring the probability that θ_μ lies in the given region R be equal to some threshold P,

$$\int_R \theta_\mu p(\theta_\mu \mid D) d\theta_\mu = P ,$$

with the probability density within R being everywhere greater than that outside it. Note that in the above discussion, we have assumed that the parameter values are continuous; in practice, the integrals turn trivially to summations because of the numerical discretization of the values.

In this work we consider only parameter estimation and not model comparison, and hence we ignore the normalization factor, which is relevant only to evaluate the relative merits of different models, e.g., sets of Θ defined for different values of n. Note that $p(D)$ serves the same function in probabilistic analysis as the partition function does in statistical physics.

5.1.2. The Markov-Chain Monte Carlo (Metropolis) Method

When the number of model parameters is large (~ 100, as here), the possible space in which the best solution exists may become too large to be computationally tractable. Such cases may be dealt with by adopting a Monte Carlo approach tempered by Markov chaining consecutive realizations to determine the best solution asymptotically (see, e.g., Nepveu 1988; Levinson 1991; Neal 1993, and references therein)

A Markov chain is an ordered sequence of random variables $\Theta_0, \Theta_1, \Theta_2, \ldots$, such that the probability of finding the system in the state Θ_{i+1} is dependent directly only on Θ_i. Each Θ_i here represents a particular realization of the model parameters: the Markov chain may be completely specified by giving the a priori distributions for the initial state Θ_0 and transition rules for going from state Θ_i to Θ_{i+1}; the latter are just conditional probabilities

$$p(\Theta_{i+1} \mid \Theta_i, \ldots \Theta_0) = p(\Theta_{i+1} \mid \Theta_i) .$$

The expectation is that such "updating" of the probabilities (formally, the probability of finding the system in the given state, as defined by Θ) would eventually cause the system to converge to an invariant probability distribution from which parameter values are sampled and which forms the solution to the inference problem. Such a process is appropriate as a searching scheme to find the (usually small) volume in the (usually large) parameter space in which the model describes the data well [e.g., where $\int p(\{\theta_v\} \mid D) d\theta_1 \ldots d\theta_N > 0.9$]. Thus when the number of parameters are large, or $p(\Theta \mid D)$ is complicated, and it may not be possible to characterize the distribution analytically, a sample of points must be drawn from $p(\Theta \mid D)$ and the distribution characterized in an approximate sense. In particular, we can obtain estimates of the probability distribution for each parameter (obtained by *marginalizing*—i.e., integrating—the full N-dimensional probability density function over the remaining parameters; see above) driving a Markov chain with a *Monte Carlo* sampling process (MCMC).

We adopt the Metropolis algorithm (Metropolis et al. 1953) as the transition rule to determine a new set of parameters (Θ^*) from an existing set (Θ):

1. SELECT a candidate set Θ^* in which all components except for a subset $\{k\}$ are the same as in Θ, while the subset

of parameters are chosen at random from a *proposal distribution* given by the probabilities $S_k(\Theta, \Theta^*)$.

2. ACCEPT the candidate set with probability $A(\Theta, \Theta^*)$; otherwise, REJECT it and retain the old set. A popular choice for $A(\Theta, \Theta^*)$ is simply the ratio of the likelihoods,

$$A(\Theta, \Theta^*) = \min\left[1, \frac{P(D \mid \Theta^*)}{P(D \mid \Theta)}\right]. \qquad (5)$$

Thus, if the new state has a higher likelihood it is accepted, and there is a finite probability that it would be accepted even if it has a lower likelihood. The latter constraint facilitates the search for the global extremum in the likelihood function.[6]

Can we be sure that this process will result in a " best-fit " solution to the problem under consideration? It is possible to show (Kemeny & Snell 1960; Neal 1993) that a Monte Carlo–driven Markov chain will converge to a persistent distribution regardless of the initial state as the number of trials increase, provided that the defined Markov chain satisfies certain plausible requirements. The first and foremost of these requirements is that there *does exist* such a persistent distribution to be found, i.e., the probability of finding the system in a given configuration—a particular set of values of Θ—will remain unchanged once this *invariant* (or *stationary*) probability distribution is realized. Second, the transition rules defining the system are assumed to not change with time (i.e., the chain is *homogeneous*).[7] Finally, the Markov chain is assumed to converge to the persistent distribution independently of the specified initial state (in other words, an invariant distribution may be reached from any valid initial state, i.e., any valid set of model parameters may be obtained with nonzero probability from any other valid set, a condition sometimes called "ergodicity"). It can then be seen that by writing the probability of a state occurring at any given step as a linear combination of the persistent distribution and another arbitrary distribution, as a Markov chain proceeds, the weight given to the invariant component must steadily increase because of ergodicity, and hence the Markov chain must converge to the invariant distribution.

Note that the convergence is stochastic, in the sense that regardless of how large the number of trials k may be, after a sufficiently large number of trials $j \gg k$, Θ_j will be nearly independent of Θ_k, though both sets will have been sampled from the same persistent probability distribution.

5.2. *Implementation*

Here we describe in detail the manner in which we implement the algorithm described above to the specific problem

of DEM inference using measured line fluxes in unambiguously identified spectral lines. In particular, we first point out the correspondence between the terms in equation (2) and the terminology of the previous section and then walk through various features of our implementation that are not a part of standard MCMC[M] approaches but are necessary for various reasons. We then list some of the advantages and shortcomings of our method.

5.2.1. *DEMs and MCMC[M]*

In the specific case of inferring a DEM, the data (D_i) are the measured line fluxes, corresponding errors, and upper limits associated with specific transitions $u \to l$. These are related to the DEM through the line contribution functions $G(T)$, as described by equation (2).

We identify the model parameters θ_v with values $\{\varepsilon(T_v), \zeta\}$, where $\varepsilon(T)$ are pseudo-DEM parameters that are defined independently at each of the n_T temperature bins, and ζ are the $\log_{10}$ abundances of elements. The actual $\mathrm{DEM}(T_v)$ are derived from a complete set of ε by *local* smoothing at scales derived from a wavelet analysis of $G_{ul}(T_v)$ (see § 5.2.3 below).

The likelihood function for a detected line of measured flux $f_i \pm \sigma_i$

$$p(D_i \mid \Theta) = e^{-1/2[f_i - f_{\mathrm{pred}}/\sigma_i]^2},$$

where f_{pred} is the flux predicted for the line for the specified DEM (see eq. [2]).[8] In contrast, where only upper limits are available, $p(D_i \mid \Theta) = 1$ if $f_{\mathrm{pred}} \leq f_i$, and 0 otherwise.

5.2.2. *Procedure*

We first specify the ranges over which $\varepsilon(T)$ and ζ may vary.[9] This is equivalent to specifying constant a priori probability distributions $p(\varepsilon(T), \zeta)$ over the allowed range. The proposal distributions S_k (cf. § 5.1.2) are initially set to be uniform over the allowed range of each parameter and are recomputed as Gaussian distributions from estimates of $p(\theta_v \mid D)$ after an initial run to achieve stabilization.

We follow a hybrid scheme for the selection and variation of parameters: if there are n parameters defining the system (this could be a combination of $\varepsilon(T)$ and ζ), then n candidate parameters are selected one at a time, a new value is determined as a deviation from the old value, the new and old likelihoods are compared, and the new value is accepted or rejected based on the Metropolis (see above) criterion. The values of T defining $\varepsilon(T)$ are sampled from an envelope $\gamma(T)$ obtained by adding together the normalized emissivity functions,

$$\gamma(T) = \sum_{\{ul\}} \frac{G_{ul}(T)}{\max[G_{ul}(T)]}, \qquad (6)$$

while the values of ζ are considered in order. Thus the emissivity functions $G_{ul}(T)$ constrain the temperatures at which the DEM may be determined—for example, no estimate of a DEM is possible at values of T where $G_{ul}(T) = 0$ for all the transitions considered. New values of a parameter θ_p are obtained by considering normal deviations $\theta_p|_{\mathrm{new}} = \theta_p|_{\mathrm{old}} + r\sigma_p$, where r is a random number and σ_p is an estimate of the variance of θ_p. The variance of each parameter

---

[6] Note that this is similar in concept to simulated annealing (Kirkpatrick, Gelatt, & Vecchi 1983; Černý 1985), which also use the Metropolis algorithm to move the solution out of local minima. However, while simulated annealing appeals to an analogy to physical processes (cf. the minimization of an "energy" function and the use of a control "temperature"), MCMC[M] has a simple statistical interpretation (maximization of the probability of the model parameters for the given data and other prior information). Indeed, MCMC methods may easily be modified to include an "annealing schedule" by, e.g., reducing the width of the proposal function gradually, as a function of the temperature of the system. Also, simulated annealing may be directly incorporated into MCMC simply by adopting the system temperature as another parameter in the problem (simulated tempering; Marinari & Parisi 1992)!

[7] Note that this excludes the process of simulated annealing or tempering, where the transition rules *do* change. Considerations of convergence in the presence of such variables is beyond the scope of this article.

[8] We have assumed normal errors here, but the algorithm may be trivially generalized to Poisson errors.

[9] If the allowed range for any one of the parameters is 0, i.e., the upper and lower limits are equal to each other, the parameter is held fixed; i.e., we impose a δ-function prior on that parameter.

may be specified a priori and is also recomputed at the beginning of the simulation, after an initial "burn-in" period. The burn-in period lasts until the frequency histograms of the values of the parameters stabilizes, as determined by comparing the current accumulated histograms (f_i) with those generated by the end of the previous batch (f'_i; see below), i.e., when the ratio

$$\left\langle \frac{\sum (f_i f'_i)^2}{\sum f_i^2 \sum (f'_i)^2} \right\rangle \qquad (7)$$

exceeds a preset value (say 0.98). Each parameter thus sampled is saved for future reference. At the end of each cycle, all the $\varepsilon(T)$ that were not sampled despite being tagged for variation are then varied all at once and the new set is also accepted or rejected according to the Metropolis criterion.

The simulations are carried out in batches, where each batch consists of a number of cycles of parameter selection. The values of $\log_{10} [\mathrm{DEM}(T)]$ [obtained by local boxcar smoothing of $\varepsilon(T)$] and ζ are stored at the end of each batch. The size of a batch is designed to ensure that the values of the parameters at the end of each batch are nearly independent of values obtained at the end of a previous batch, so that errors on the parameters may be easily estimated (cf. Geyer 1993; Gelman & Rubin 1993). (In practice, we find that a batch consisting of 10 cycles—i.e., when a typical parameter value is 10 times removed from an earlier realization—is adequate.) At the end of the simulation run, the distribution of values of $\log [\mathrm{DEM}(T)]$ and ζ are used to determine the confidence intervals (as a deviation from the best solution that includes a set fraction of the stored points). This process is equivalent to sampling from $p(\theta_v | D)$, obtained by marginalizing over all the other parameters.

5.2.3. Smoothing

As discussed in § 3, it is necessary to introduce a smoothness criterion to a DEM solution. In order to avoid imposing an arbitrary and inflexible criterion, we use the line emissivity functions $G_{ul}(T)$ (cf. § 3) to compute characteristic scales $[L_{ul}(T)]$ for each transition that determines the *local* scales over which DEM must be smoothed:[10] the smallest scale determined at each T for the various transitions constrains the local structure of the DEM. In this way, we optimize the smoothing to obtain the maximum amount of structural detail in the DEM. We determine the local scale by correlating $G_{ul}(T)$ with the Mexican Hat wavelet

$$\frac{1}{\delta}\left[1 - \left(\frac{\log T}{\delta}\right)^2\right] e^{-[(\log T)^2/2\delta^2]} \qquad (8)$$

at numerous scales δ. The value of δ for which the response of $G_{ul}(T)$ to the Mexican-Hat function is maximum determines the local length scale $L_{ul}(T) = 2\delta$. The model parameters $\varepsilon(T)$ are boxcar-smoothed locally at these scales to generate predicted values of $\log_{10} [\mathrm{DEM}(T)]$.[11]

5.2.4. Advantages and Disadvantages

Here we discuss the various strengths and shortcomings of the algorithm we have developed to infer differential emission measure distributions from observed spectral lines; the points mentioned apply not just to the MCMC[M] method but to the implementation as a whole.

First, we note that, *like any existing DEM reconstruction technique*, our algorithm cannot rigorously handle errors in the atomic data, i.e., the computed confidence limits do not include possible errors in line strengths, level populations, or ionic fractions (see § 3.2). However, we have tested the algorithm by approximating these errors (cf. § 3 and the Appendix) and find that it does not significantly affect the results of the reconstruction. Further, the fine structure in the reconstruction is also limited by the widths and the number of the line contribution functions $G_{ul}(T)$, but the required smoothing does not preclude sharp features (Kashyap & Drake 1997), and we do not impose any global smoothness criteria on the solution.

The main strength of our technique is that it provides confidence limits on the most probable DEM, thus allowing a determination of the significance of apparent structures that may be found in a typical reconstruction. As can be seen from Figure 1, this is a crucial component of any DEM reconstruction[12] and follows directly from the mathematical basis of the algorithm (§ 5.1.2). The same mathematical structure also allows us to include censored data (in the form of upper limits to line fluxes) in a trivial way in the reconstruction, thus allowing the DEM to be characterized even at temperatures at which no detectable lines have formed. Further, our specific dependence on the machinery of MCMC implies that the final result is independent of the initial conditions as long as the prior imposed on the problem is not too restrictive (e.g., large errors may result in the reconstruction if the allowed range of parameter values is constrained to too small a range in the presence of censored data). However despite its power the same mathematical structure also imposes certain limitations, the most important of which is that comparison of different *types* of DEM models, e.g., those obtained with different temperature bin sizes or with different parameterizations (such as Chebychev polynomials), are not directly comparable without extensive calculations (cf. Loredo 1990)—this is because model comparisons involve $p(D)$, the normalization factors in equation [4], which may be difficult to estimate when the number of parameters is large.

In practice, we find that our technique is easily adaptable to varying numbers of parameters in the problem and is especially well suited for problems with a large number of parameters (~ 100). The numerical overhead of course increases directly as the number of parameters, and convergence may sometime be slow, but note that the algorithm may easily be parallelized if needed.

Finally, we note that local extrema in the likelihood function will not trap the solution (cf. § 5.1.2), a trait also shared

---

[10] It can be argued that our method is based only on the *lack of* information as encoded in the kernel $G(T)$ of equation (2). Note however that this does constitute a *physical* constraint, as opposed to artificially imposed mathematical constraints such as polynomial fitting. In that sense, and only to that extent, we note that this type of smoothing is physically meaningful.

[11] Thus the positivity constraint on the DEM is automatically enforced.

[12] While it is not our intention here to compare our technique with other optimization methods, such as simulated annealing (Kirkpatrick et al. 1983; Černý 1985; Marinari & Parisi 1992), genetic algorithms (Charbonneau 1995), or others (see Kaastra et al. 1996a), we should note that none of these techniques provide a natural means to estimate the statistical errors on the reconstructed DEM. Even in the case of genetic algorithms, where the distribution of parameter values at the end of a run may be used to illustrate these errors, there is no guarantee in principle that this spread corresponds to the statistical error on the best-fit values.

by other sophisticated optimization techniques such as simulated annealing or genetic algorithms.

6. RESULTS AND DISCUSSION

6.1. *Reconstructed DEMs*

We apply the MCMC[M] algorithm outlined above (§ 5; also, Kashyap & Drake 1998) to the spectral line lists of B96 corresponding to AR93 and QS93 in order to derive the DEMs. We emphasize again that, because we use different atomic line data, ion balance calculations and abundances [§ 4.2.2; the lower photospheric abundances of the low-FIP elements result in higher estimates of DEM(T)], as well as avoid global smoothing of the DEM, we expect at the outset that the DEMs derived here will be different from those derived by B96. Also, in order to explore the sensitivity of the reconstruction to the spectral lines used, we derive DEMs for (1) the same set of lines as used by B96 in their DEM inversions (Fig. 2); (2) the full data set, but excluding some lines as discussed above in § 4.2.3 (Fig. 3); and (3) the full data set (with excluded lines) with additional upper limits (Fig. 4).

Reconstructed DEMs for the various line data sets are shown in Figures 2, 3, and 4, for line sets [a] (the same lines as used by B96), [b] (all the lines in the SERTS database except those excluded in § 4.2.3), and [c] (the same as [b], but including the undetected lines in Table 1), respectively. The error bars correspond to 2 σ limits and were calculated by a Monte Carlo sampling from the posterior distribution $p(\Theta \mid D)$ (cf. eq. [4]). These DEMs, taking into account the uncertainties at each temperature, are as expected clearly different from the DEMs constructed by B96.

The DEMs derived from data set [a] (Fig. 2) show evidence of double-peaked structures in both the AR93 and QS93 cases, but unlike the DEMs derived by Brosius et al. (1996) (note however that the second peak in the QS93 DEM is not statistically significant). Further, the peaks in

FIG. 3.—As in Fig. 2, but derived from the full SERTS line list except those lines listed in § 2 (data set [b]).

the AR93 case are at lower temperatures. Note that the dip at $10^{6.2}$ K is not significant when compared to the adjacent bins. The DEMs are not defined below $10^{5.6}$ and above $10^{6.8}$ K because of the lack of spectral lines in the data set that cover the appropriate temperature regions. With this set of spectral lines, we are thus unable to confirm the location of the DEM minimum, which in the solar corona is generally found near log $T \sim 5$, and the drop in the DEM at high temperatures.

The extended set of lines in data set [b] lead to DEMs (Fig. 3) that are qualitatively similar but show some interesting differences. First, the peaks in the active-region DEM now lie at lower temperatures than before; second, there is evidence of a peak at $\sim 10^{6.6}$ K (the apparent peak at $10^{5.8}$ K is clearly not significant, based on the large error bar associated with it); third, the minimum of the DEM is located between $\sim 10^{5.4-5.7}$ K (but the poor spectral coverage of this temperature range implies that this result could be sensitive to systematic errors; cf. § 3.2).

Inclusion of undetected lines that contribute at high temperatures (data set [c]; Fig. 4) allows us to extend the DEM past 10^7 K. The upper limits are however not stringent
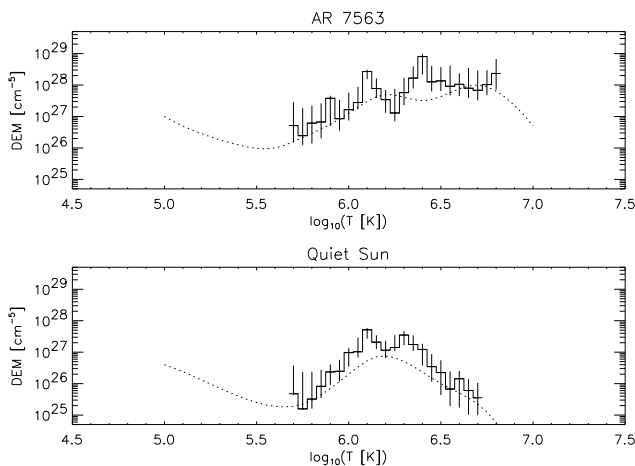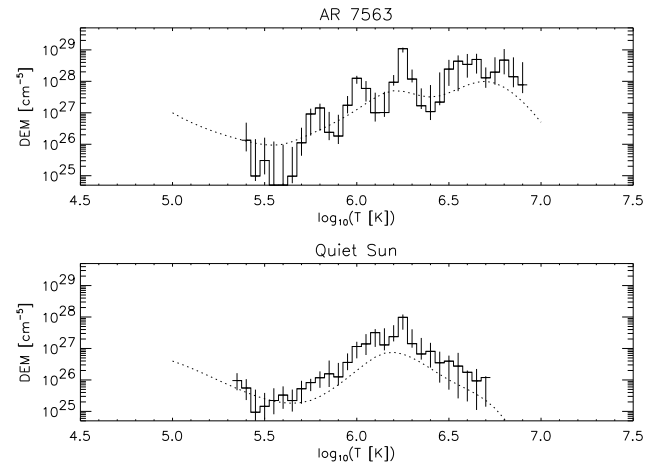

FIG. 2.—Active- (*upper panel*) and quiet-Sun (*lower panel*) region DEMs (*stepped line*) derived with the MCMC[M] technique, assuming solar photospheric abundances recommended by Grevesse et al. (1992), involving 500 simulations point^{-1} and using the same line list as used by Brosius et al. (1996). Electron densities of 10^9 and 5×10^9 cm^{-3} were assumed for the quiet Sun and active regions, respectively. Where line information is absent, the DEM is not well determined and is not shown here. The dotted lines show the DEMs derived by Brosius et al. (1996). The widths of the steps indicate the widths of the temperature bins and the vertical bars denote 95% confidence limits on the derived DEM(T).
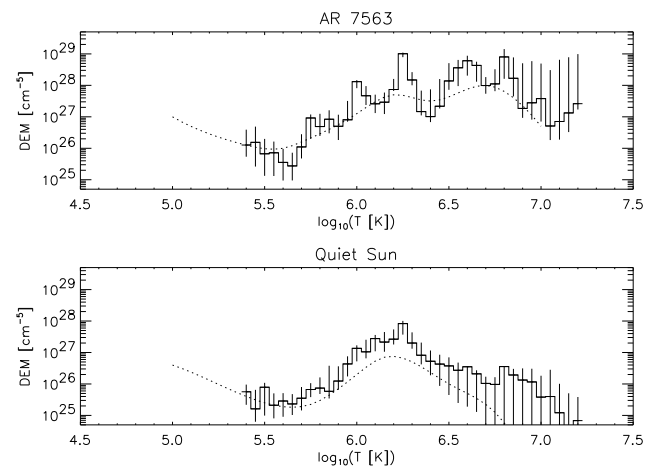

FIG. 4.—As in Fig. 2, but derived from the full SERTS line list excluding certain lines and including upper limits from high-temperature lines (cf. § 2; data set [c]).

enough to allow us to conclude whether the active-region DEM shows a downturn (we are able to conclude that there is no upturn in the quiet-Sun DEM at high temperatures!). As expected, there are no structural changes at lower temperatures compared to data set [b].

The quality of the reconstruction may be judged by Figure 5, which compares the predicted and observed fluxes for line set [b]. The majority of the predicted fluxes are within a factor of 2 of the observed fluxes, indicating that the residual scatter is due to the systematic uncertainties inherent in the data (§ 3.2), possibly including errors in the underlying assumptions (§ 3). This is supported by the large spread in the deviations of lines at a given temperature, which ought to be relatively insensitive to the details of the reconstruction algorithm.

We have also explored the effect on the reconstructed DEM of varying the abundances. During the reconstruction, we simultaneously fit the abundances of lines in data set [b] relative to Fe (we cannot determine the absolute abundances because we cannot then constrain the normalization of the EM), and we find that there are no significant changes to the DEM compared to that in Figure 3. This is a result of the relatively small changes (indeed, except for Si, consistent with *no* changes; Fig. 5) in the best-fit abundances of the low-FIP elements relative to the adopted abundance of Fe (see § 4.2.2). The large discrepancy in the relative abundance of Ne is due to the lack of any constraints on it other than from Mg (see § 4.2.2; also see Fig. 1).

6.2. *Implications for Physical Inference from DEM Inversions*

The most striking aspect of our reconstructed DEMs is the amount of apparent structure, especially in the AR93 reconstructions. These are markedly different to the smooth spline or power-law type of relationship generally found in DEM or EM inversions of solar spectra (e.g., see the flare EM distributions of Dere & Cook 1979; the quiet-Sun EM distributions of Raymond & Doyle 1981; the active-region DEM derived by Dere 1982; or the active- and quiet-Sun DEMs of B96). Indeed, we have also performed experiments to test whether or not the structure in these DEMs reproduces the observed line fluxes significantly better than do the smooth DEMs described by Chebychev polynomials. In these experiments, the DEM at each point in the temperature grid was simply parameterized by polynomial coefficients rather than allowed to vary quasi-independently (neighboring bins are related through the imposed global smoothing), and the reconstruction proceeded in an identical manner under our MCMC[M] algorithm. In both the AR93 and QS93 cases, the overall fit to the observed fluxes as indicated by the χ^2 statistic was dramatically degraded (by greater than factors of 2) by the imposition of globally smooth solutions.

The main scientific issue resulting from this study is, then, whether or not this structure in the emission measure is real: whether it is in the EUV-emitting source itself, or whether it is imposed on a more smooth distribution by
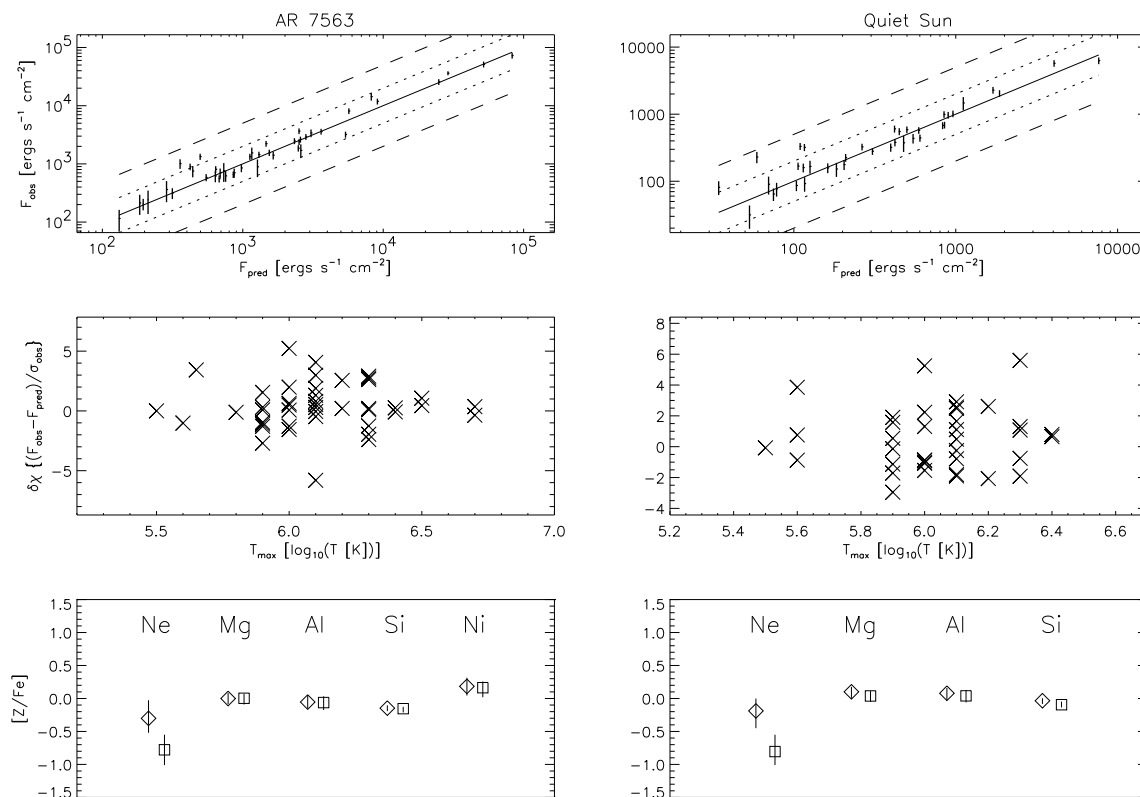

FIG. 5.—Quality of the DEM reconstruction, for data set [b]. The plots in the left panels describe the active-region DEM, while those in the right panels describe the quiet-Sun DEM. The upper panels compare the observed and predicted fluxes: the solid line represents $F_{observed} = F_{predicted}$; the dotted and dashed lines represent factors of 2 and 5 departures from equality, respectively; and the solid vertical lines show the 2 σ error bars on the observed fluxes. The middle panels show the temperature coverage of the lines and the quality of the fit to each line: the scatter at a given temperature must be ascribed to uncertainties in the atomic data and/or breakdown of assumptions. The lower panels show the results of allowing abundances to vary relative to Fe. The diamonds and squares represent baseline Fe abundances from Grevesse et al. (1992; photospheric) and Feldman et al. (1992; coronal), respectively; the solid vertical lines indicate 95% confidence limits on the estimates.

some errors in the various ingredients that enter into the DEM reconstruction.

A convincing case for the latter hypothesis might be made on the grounds that the different data sets yield significantly different solutions: the DEM derived from data set [b], which includes the full set of B96 lines other than those excluded for reasons discussed in § 4.2.3, exhibits peaks and troughs at different temperatures than the DEM derived from data set [a]. While it is clear that the *differences* between the two DEMs are simply caused by the different sets of spectral lines employed, it is not so straightforward to rule out any spurious features in the DEM derived from the smaller data set ([a]). One clue is perhaps provided by the individual ion EM points in Figure 1: the dip near $\log T \sim 6.25$ is a consequence of the Fe XIII point, while the shift in the peak at $\log T = 6.4$ appears to be due to the exclusion of the S XII line.

An interesting comparison to make is between the AR93 and QS93 DEM reconstructions. Based on the set of lines [a], our reconstructions together with their confidence limits suggest these to be statistically identical for $\log T < 6.4$ or so, except for a small normalization offset. Above this temperature, the AR93 DEM clearly extends toward higher temperatures than that for QS93. The B96 reconstructions, at face value, seem to suggest that QS93 has a steeper EM slope than AR93 for $5.5 < \log T < 6.2$. It is only when the uncertainties in the DEM are considered that this apparent difference in slope is shown not to be significant.

In the case of data sets [b] and [c] (Figs. 3 and 4, respectively), we are again drawn to remark on the local maximum near $\log T \sim 6.0$ in the AR93 reconstruction, which does not appear in the corresponding QS93 reconstruction.

As in other areas of spectroscopy, the key to success in our opinion lies in the careful choice of the input spectral indices used in the DEM reconstruction. Here we are assuming of course that the underlying assumptions involved in the calculation of a DEM (cf. § 3) are valid. Spectral lines must be both well observed and also have well-known theoretical line strengths. Ideally, lines from different elements should not be used to infer DEM structure because of inevitable uncertainties in relative abundances. For example, it is extremely unlikely that in the stellar case the coronal (and photospheric) abundances in a coronally active star are going to be known to better than 0.1 dex—a number comparable to the likely uncertainties in theoretical line strengths for reasonably well-studied ions (see, e.g., Laming et al. 1995). As we see in our reconstructions based on high-quality solar data, differential studies based on different sets of observations will be extremely difficult in anything other than the gross sense unless the observed spectral indices (usually the spectral line list) are the same.

We are sobered by the somewhat negative conclusion of Craig & Brown (1976) and Judge et al. (1997) in regard to what one might learn of the temperature structure of the corona from integral inversion analyses of spectral line intensities: they suggest that very little may be deduced about the source term based on this type of data, regardless of its quality. However, we also wonder whether or not this conclusion might have been colored by application to the solar case in which differences in the "structure of the source term" in different coronal regions and features are actually relatively small when compared to the much wider

range of stellar parameter space. In the stellar case, while the observational data is, and will be, of considerably lesser quality, the differences in coronae from star to star can be quite gross as one can immediately see from their spectra (see, e.g., Brown 1994). DEM reconstruction (our term for the forward approach to the problem we adopt here in distinction to the inverse problem) still offers a useful comparison tool (provided the corollaries mentioned above are considered) and a first-order empirical, one-dimensional model from which further physical insight can be gleaned more easily and intuitively, as pioneered by workers such as Jordan (1980, and references therein).

6.3. Coronal Structure

Observations of the solar corona with instruments aboard various telescopes (*Skylab*: Vaiana et al. 1973; *NIXT*: Golub et al. 1990; *Yohkoh*: Acton et al. 1992; *SOHO*: Domingo, Fleck, & Poland 1995) have shown that X-ray emission is highly inhomogeneous and arises in loop-like structures arranged in complex configurations. It is widely recognized that the geometry of these loops is dictated by the structure of the coronal magnetic field (see, e.g., Rosner et al. 1985; Litwin & Rosner 1993) and that the X-ray structures are magnetic flux tubes filled with hot coronal plasma. The structure of the plasma in each individual loop is also complex (Kano & Tsuneta 1996; Tsuneta 1997), but the loops have been successfully modeled as hydrostatic, energy-balanced, one-dimensional structures (Rosner et al. 1978; Serio et al. 1981; Kano & Tsuneta 1995; see also Porter & Klimchuk 1995 for a different viewpoint).

DEMs derived from such loops are not smooth but rather are discontinuous, with a sharp increase up to the maximum loop temperature (T_{max}) as the temperature gradient along the loop drops rapidly. Such temperature structures are much narrower than the limitations imposed on DEM reconstruction by the atomic line contribution functions $G(T)$ (cf. § 3). Moreover, the solar corona is highly inhomogeneous, and many loops, each with a different T_{max}, would contribute to the observed intensities in spectral lines. Thus we would not expect to observe sharp peaks in the reconstructed DEM. However, our reconstruction of the solar DEM shows many local enhancements, which we may identify with distinct loop families—i.e., we speculate that the features in the DEM distributions arise from a complex of loops similar in size (and hence temperature and emission measure) seen along the line of sight. We may then derive loop properties from the observed DEM and compare these with the expected theoretical properties. The results of such calculations are listed in Table 3.

Comparing the derived loop height (cf. Table 3) with the height predicted by the coronal loop scaling law [$T_{max} = 1.4 \times 10^3 (pL)^{1/3}$, where p is the base pressure and L is the loop semilength; Rosner et al. 1978], we see that the peaks in the active-region DEMs deemed significant (see § 6.1) are indeed consistent with features arising in individual coronal loops, whereas peaks that are not well defined—features at low or high temperatures, in both AR93 and QS93 DEMs—are inconsistent with simple loop structures. Whether this departure from the scaling law arises from a breakdown in the form of the conductive and radiative fluxes or in the form of the heating involved (cf. Porter & Klimchuk 1995), or whether the X-ray emitting structures at such temperatures may not be regarded as loops, we cannot say based on our data set.

| LINE DATASET | $\log_{10}(T)$ (K) | HEIGHT (cm) | |
		Observed[a]	Predicted[b]
AR93 [a]	5.9	$(0.8–4) \times 10^7$	2.1×10^8
	6.1	$(4–8) \times 10^8$	5.3×10^8
	6.4	$(0.4–2) \times 10^9$	2.1×10^9
AR93 [b]	5.8	$(0.5–2) \times 10^7$	1.3×10^8
	6.0	3×10^8	3.4×10^8
	6.25	1.6×10^9	10^9
	~ 6.6	$(1–2) \times 10^9$	$(3–5) \times 10^9$
	~ 6.8	$(5–8) \times 10^8$	$\sim 10^{10}$
QS93 [b]	6.0–6.3	$\sim 2 \times 10^9$	$\sim 5 \times 10^9$

[a] Height of emitting structure derived from the reconstructed DEM.

[b] Predicted height of loop from scaling law, uncorrected for projection.

The geometry of the quiet-Sun corona is not as well determined. *Yohkoh* observations (Sturrock, Wheatland, & Acton 1995; Wheatland, Sturrock, & Acton 1997; Foley, Culhane, & Acton 1997; Tsuneta 1997) show that the mean temperatures are much lower than in the active region (as is borne out by our reconstruction, which shows a maximum at $6 < \log T < 6.3$) and that the temperature tends to increase with height above the surface. The height we calculate from the QS93 DEM (Table 3) is consistent with the height of maximum emission measure (Sturrock et al. 1995; Foley, Culhane, & Acton 1997). Note that this height is also consistent with that derived from an energy-balanced hydrostatic model, suggesting that the quiet corona may indeed be composed of plasma-filled loops in hydrostatic equilibrium. The significance of this result is however limited by the uncertainty in the magnetic structure in the quiet corona (while closed field lines are indeed observed, a strong radial component is almost certainly present, and no information is available regarding filling factors) and consequent uncertainty in the validity of any scaling laws (Klimchuk & Gary 1995; Porter & Klimchuk 1995; Wheatland et al. 1997).

We speculate that the broad feature at $6.5 < \log T < 6.7$ in AR93 DEMs arises as a superposition of the DEMs of many individual loops; indeed, this view is supported by an image of NOAA AR 7563 obtained with the *Yohkoh* SXT (Tsuneta et al. 1991; this instrument has peak response at 5×10^6 K), which shows a large complex of loops of various sizes arranged laterally. Conversely, if individual loops may be discerned via structures in the EM distribution, it implies that there are very few loops at lower temperatures (10^6–3×10^6 K) in the active region under study, suggesting a distinct loop population with lower maximum temperatures. This is contrary to the conclusions of Yoshida et al. (1995), who compared simultaneous observations of the solar corona away from active regions performed with *Yohkoh* and *NIXT* (Golub & Herant 1989): they find that any morphological differences in the images may be explained as due to the differences in the temperature responses of the two instruments—e.g., *NIXT* observes the lower portions of coronal loops whose hot components are more easily seen with *Yohkoh*. Our DEM reconstruction however implies that (1) individual coronal loops exist even at such low maximum temperatures as 1 MK, (2) the variation in loop properties is larger for high-temperature loops than for the low-temperature loops, and (3) there are X-ray emitting structures that are inconsistent with a simple loop model in both the active and quiet-Sun regions.

7. SUMMARY

We have investigated and discussed from an empirical point of view the reconstruction of coronal differential emission measure distributions. We have described a new method, based on a Markov-chain Monte Carlo algorithm, to solve the forward problem of determining the DEM that best fits a set of observed spectral lines fluxes, upper limits to observed fluxes (censored data), and other arbitrary source parameters such as elemental abundances. Our method is suitable for problems involving a large number of free parameters and enables realistic estimation of the final uncertainties on the derived results.

Using the SERTS EUV spectral line observations presented by B96, we have reconstructed the DEMs that best fit the observations. The most striking aspect of the results is the large amount of structure in the DEMs. Our DEMs with this structure reproduce the observed line fluxes substantially better than do any smooth solutions based on low- to moderate-order polynomials, splines, or like functions.

We discuss the reality of the results from a statistical viewpoint: the confidence ranges we place on the DEMs allow us to identify which of the derived structures are significant (indeed, without this measure of uncertainty, the reconstruction would be quite useless, and possibly misleading). For example, the apparent feature at $10^{5.8}$ K in AR93 (Fig. 3) is consistent with a monotonically rising DEM, and the double peaked structure in QS93 is consistent with a broad maximum—conclusions made possible solely by the error bars associated with the values. Further note that structure in the DEM may be driven by errors in the underlying assumptions or in the atomic data (cf. § 3), and a careful consideration of the ingredients in the DEM reconstruction is necessary to avoid spurious results. In that regard, note that the overall shapes of the reconstructed DEMs (cf. structures deemed significant, such as the double peaks in AR93 and the decrease toward a minimum near $10^{5.5}$ K in both AR93 and QS93, etc.) are quite robust to changes in the adopted line lists, even though the *locations* and *magnitudes* of the features may vary considerably; the combination of robustness to different groups of lines as well as statistical significance allows us to conclude that these structures are not spurious. This study thus demonstrates the limits of the applicability of the DEM set by the scatter caused by atomic data and possible invalidity of the underlying assumptions (cf. Fig. 1).

We speculate that the observed structure might correspond to the individual loops, or families of loops, visible in *Yohkoh* soft X-ray images of the solar coronal region corresponding to the SERTS spectral observations and show that the prominent features in the DEM are consistent with loops.

KASHYAP & DRAKE

APPENDIX

SIMULATIONS

Here we demonstrate the MCMC[M] algorithm by reconstructing DEMs from simulated data sets. We generated line lists in the 300–400 Å range (similar to SERTS) using the CHIANTI database (Dere et al. 1997) for prespecified DEMs and chose a small subset of the available lines (typically 50 of the strongest lines, but excluding He II λ303) from which to reconstruct the DEM. Assuming a Gaussian error as a certain constant fraction of the predicted flux, we obtained a new set of fluxes as random normal deviations from the calculated fluxes, using the assumed errors. In addition, we also included lines with peak contributions at various temperatures from $10^{6.8}$ to 10^8 K; this set of lines are treated as upper limits, with the limit assigned arbitrarily as the largest line flux obtained for this set.

The results of the simulations are shown (see Figs. 6, 7, and 8) for DEMs of the type used by Harrison & Thompson (1991) to test integral inversion methods; in all cases, we have computed the line emission at a constant pressure of 10^{16} cm^{-3} K^{-1}, for solar photospheric abundances (Grevesse et al. 1992). The temperature coverage of the lines included in the analysis is also shown. The MCMC[M] method clearly reproduces the major structures in the DEMs even when the noise is significant. The value of the method is also illustrated in the confidence limits, without the existence of which apparent structures in the "best-fit" DEM would be overinterpreted. Also note that the line fluxes predicted by the reconstructed DEM closely match the simulated fluxes (generally to much better than factors of 2; the quality of the "best-fit" solutions is equivalent to a reduced $\chi^2 \sim 1$).

A point to note while considering censored data is that the reconstruction is sensitive to the a priori range in DEM(T) at the temperatures that are sensitive to the censored data points; setting too small a range may adversely affect the reconstruction at other temperatures, an effect that may be seen in Figure 7 in the form of larger error bars in the case involving upper limits.
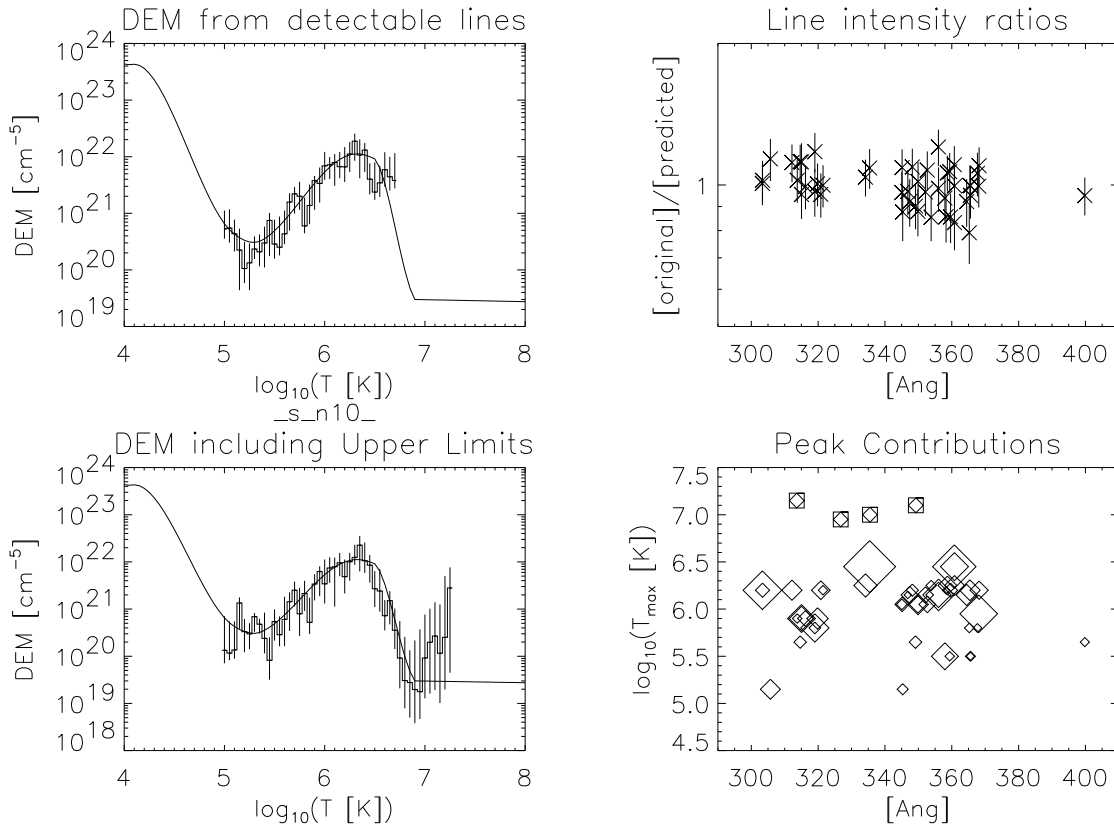

FIG. 6.—Reconstruction of a test DEM from simulated data with 10% errors. The upper left panel shows the DEM reconstructed using only "detectable" lines (*thin stepped lines*, with 90% confidence limits shown with vertical bars) along with the original DEM (*solid curve*); the lower left panel shows the same DEM reconstruction as above, but including upper limit data. The upper right panel shows the ratios of the observed (i.e., simulated) fluxes to the fluxes predicted by the reconstructed DEM. The lower right panel is a scatter plot of the wavelength of each line vs. the temperature at which the line has the maximum contribution; the relative strengths of the lines are indicated by the sizes of the diamonds, and the upper limits are marked by open squares.
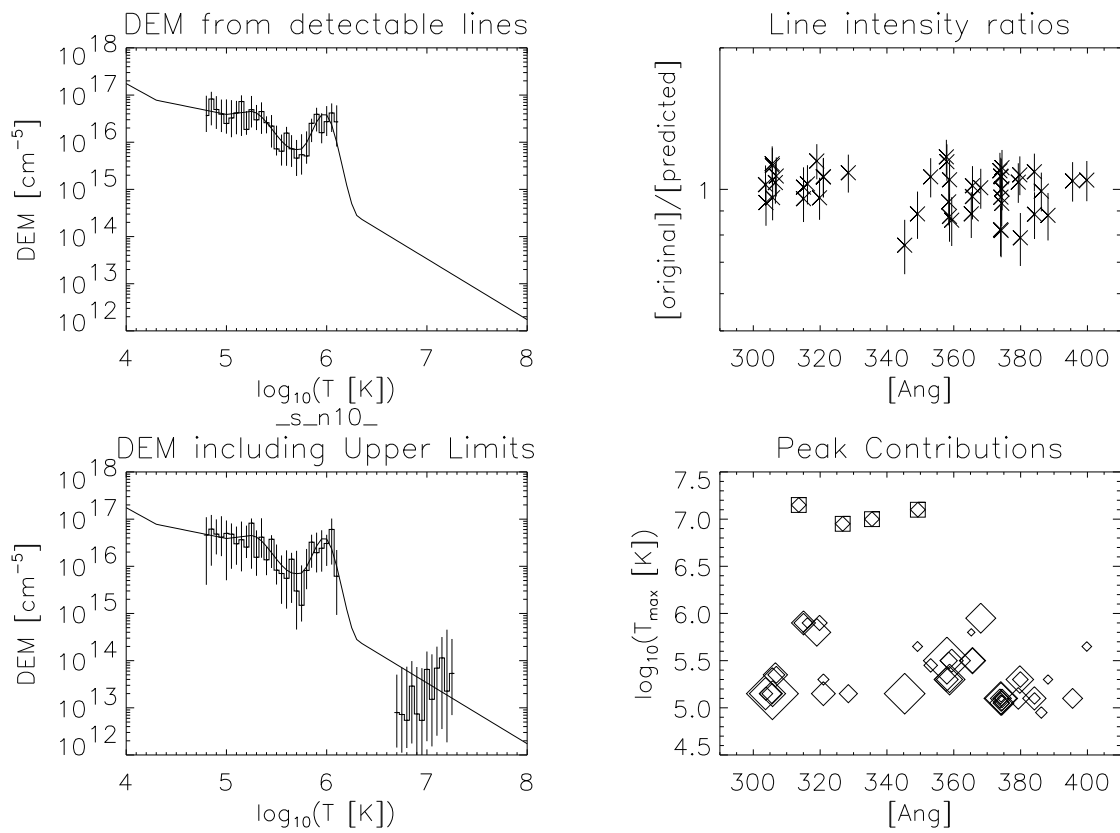
DEM from detectable lines

Line intensity ratios

DEM including Upper Limits

_s_n10_

Peak Contributions

Fig. 7.—As in Fig. 6, for a different test DEM

DEM from detectable lines

Line intensity ratios

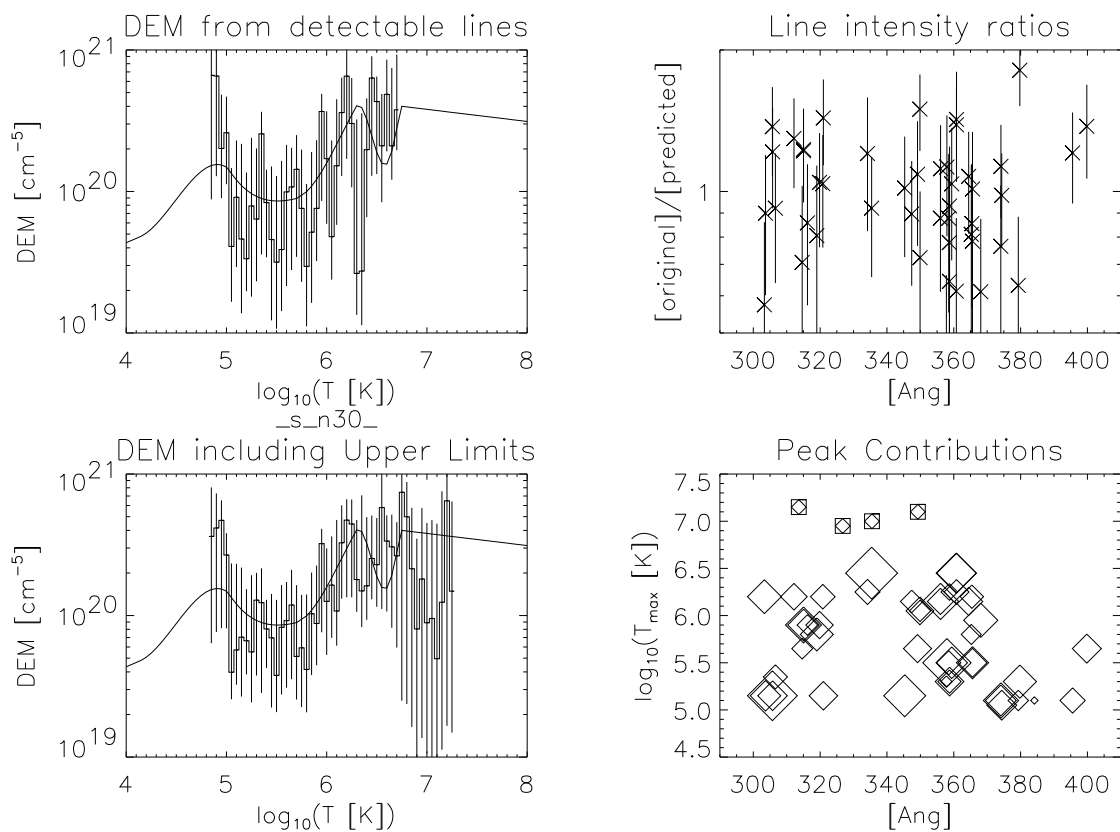## DEM including Upper Limits

_s_n30_

Peak Contributions

Fig. 8.—As in Fig. 6, for a different test DEM and assuming 30% errors. While the general shape of the input DEM is rederived, the fine structure cannot be reconstructed in the presence of large measurement errors.

REFERENCES

Acton, L., et al. 1992, Science, 258, 618
Aggarwal, K. M. 1984, ApJS, 54, 1
Aggarwal, K. M., Berrington, K. A., Kingston, A. E., & Pathak, A. 1991, J. Phys. B, 24, 1757
Aggarwal, K. M., Callaway, J., Kingston, A. E., & Unnikrishnan, K. 1992, ApJS, 80, 473
Arnaud, M., & Raymond, J. C. 1992, ApJ, 398, 39
Arnaud, M., & Rothenflug, R. 1986, A&AS, 60, 425
Berrington, K. A., & Pelan, J. 1995, A&AS, 114, 367
Bhatia, A. K., & Doschek, G. A. 1992, At. Data Nucl. Data Tables, 52, 1
———. 1993, At. Data Nucl. Data Tables, 55, 315
———. 1995, At. Data Nucl. Data Tables, 60, 145
Bhatia, A. K., Kastner, S. O., Keenan, F. P., Conlon, E. S., & Widing, K. G. 1994, ApJ, 427, 497
Bhatia, A. K., & Mason, H. E. 1980, MNRAS, 190, 925
Brickhouse, N., et al. 1995, Legacy, 6, 4
Brosius, J. W., Davila, J. M., Thomas, R. J., & Monsignori-Fossi, B. C. 1996, ApJS, 106, 143 (B96)
Brown, A. 1994, in ASP Conf. Proc. 64, Cool Stars, Stellar Systems and the Sun, 8th Cambridge Workshop, ed. J.-P. Caillault (San Francisco: ASP), 23
Bruner, M. E., & McWhirter, R. W. P. 1988, ApJ, 326, 1002
Burke, V. M., & Lennon, D. J. 1994, A&AS, 103, 273
Černý, V. 1985, J. Optimization Theor. & Appl., 45, 41
Charbonneau, P. 1995, ApJS, 101, 309
Craig, I. J. D., & Brown, J. C. 1976, A&A, 49, 239
———. 1986, Inverse Problems in Astronomy (Bristol: Adam Hilger)
Dammasch, I. 1991, in Intensity Integral Inversion Techniques: A Study in Preparation for the SOHO Mission, ed. R. A. Harrison & A. M. Thompson, SERC Tech. Rep. RAL-91-092 (Oxfordshire, UK: Rutherford Appleton Lab.), 25
Dere, K. P. 1982, Sol. Phys., 77, 77
Dere, K. P., & Cook, J. W. 1979, ApJ, 229, 772
Dere, K. P., Landi, E., Mason, H. E., Monsignori-Fossi, B. C., & Young, P. R. 1997, A&AS, 125, 173
Domingo, V., Fleck, B., & Poland, A. I. 1995, Sol. Phys., 162, 1
Drake, J. J. 1996, in ASP Conf. Proc. 109, Cool Stars, Stellar Systems, and the Sun, 9th Cambridge Workshop, ed. R. Pallavicini & A. K. Dupree (San Francisco: ASP), 203
Drake, J. J., Laming, J. M., & Widing, K. G. 1995, ApJ, 443, 393
———. 1997, ApJ, 478, 403
Dufton, P. L., & Kingston, A. E. 1991, Phys. Scr., 43, 386
Falconer, D. A., Davila, J. M., & Thomas, R.J. 1997, ApJ, 482, 1050
Fawcett, B. C., & Mason, H. E. 1989, At. Data Nucl. Data Tables, 43, 245
Feldman, U. 1992, Phys. Scr., 46, 202
Feldman, U., Mandelbaum, P., Seely, J. F., Doschek, G. A., & Gursky, H. 1992, ApJS, 106, 143
Flower, D. R. 1977, A&A, 54, 163
Foley, C. R., Culhane, J. L., & Acton, L. W. 1997, ApJ, 491, 933
Gelman, A., & Rubin, D. B. 1993, Stat. Sci., 7, 457
Geyer, C. J. 1993, Stat. Sci., 7, 473
Golub, L., & Herant, M. 1989, Proc. SPIE, 1160, 629
Golub, L., et al. 1990, Nature, 344, 842
Gregory, P. C., & Loredo, T. J. 1992, ApJ, 398, 146
———. 1996, ApJ, 473, 1059
Grevesse, N., Noels, A., & Sauval, A. J. 1992, in Coronal Streamers, Coronal Loops, and Coronal and Solar Wind Composition, Proc. 1st SOHO Workshop, ESA SP-348, ed. C. Mattock (Noordwijk: ESA), 305
Harrison, R. A., & Thompson, A. M. 1991, in Intensity Integral Inversion Techniques: a Study in Preparation for the SOHO Mission, SERC Tech. Rep. RAL-91-092 (Oxfordshire, UK: Rutherford Appleton Lab.)
Jeffries, J. T., Orral, G. Q., & Zirker, J. B. 1972, Sol. Phys., 22, 307
Jordan, C. 1976, Philos. Trans. Roy. Soc. London A, 281, 391
———. 1980, A&A, 86, 355
———. 1992, Mem. Soc. Astron. Italiana, 63, 605
Jordan, C., & Linsky, J. 1987, in Exploring the Universe with the IUE Satellite, ed. Y. Kondo & W. Wamsteker (Dordrecht: Reidel), 259
Judge, P. G., Hubeny, V., & Brown, J. C. 1997, ApJ, 475, 275
Kaastra, J. S., Mewe, R., Liedahl, D. A., Singh, K. P., White, N. E., & Drake, S. A. 1996a, A&A, 314, 547
Kaastra, J. S., Mewe, R., & Nieuwenhuijzen, H. 1996b, in UV and X-ray Spectroscopy of Astrophysical and Laboratory Plasmas, ed. K. Yamashita & T. Watanabe (Tokyo: Univ. Acad.), 411
Kano, R., & Tsuneta, S. 1995, ApJ, 454, 934
———. 1996, PASJ, 48, 535
Kashyap, V., & Drake, J. J. 1997, paper presented at the High-Energy Astrophysics Division meeting of the AAS, Estes Park, CO (unpublished)
———. 1998, in ASP Conf. Proc., High-Resolution Solar Atmospheric Dynamics Workshop, ed. E. Deluca & J. Bookbinder (San Francisco: ASP), in press

Kemeny, J. G., & Snell, J. L. 1960, Finite Markov Chains, (New York: Springer)
Kirkpatrick, S., Gelatt, C. D., & Vecchi, M. P. 1983, Science, 220, 671
Klimchuk, J. A., & Gary, D. E. 1995, ApJ, 448, 925
Laming, J. M., Drake, J.J., & Widing, K. G. 1995, ApJ, 443, 416
———. 1996, ApJ, 462, 948
Lang, J., Mason, H. E., & McWhirter, R. W. P. 1990, Sol. Phys., 129, 31
Levinson, H. F. 1991, AJ, 102, 787
Litwin, C., & Rosner, R. 1993, ApJ, 412, 375
Loredo, T. J. 1990, in Maximum Entropy and Bayesian Methods, ed. P. F. Fougere (Dordrecht: Kluwer), 81
Marinari, E., & Parisi, G. 1992, Europhys. Lett., 19, 451
Mariska, J. T. 1992, The Solar Transition Region, (Cambridge: Cambridge Univ. Press)
Metropolis, N., Rosenbluth, A. W., Rosenbluth, M. N., Teller, A. H., & Teller, E. 1953, J. Chem. Phys., 21, 1087
Mewe, R., Kaastra, J. S., Schrijver, C. J., van den Oord, G. H. J., & Alkemade, F. J. M. 1995, A&A, 296, 477
Meyer, J.-P. 1985, ApJS, 57, 173
Monsignori-Fossi, B. C., & Landini, M. 1991, in Intensity Integral Inversion Techniques: A Study in Preparation for the SOHO Mission, ed. R. A. Harrison & A. M. Thompson, SERC Tech. Rep. RAL-91-092 (Oxfordshire, UK: Rutherford Appleton Lab.), 27
———. 1994, Sol. Phys., 152, 81
Neal, R. M. 1993, Technical Report CRG-TR-93-1, Dept. Comput. Sci., Univ. Toronto
Nepveu, M. 1988, A&A, 193, 173
Neupert, W. M., Epstein, G. L., Thomas, R. J., & Feldman, U. 1981, Space Sci. Rev., 29, 425
Pelan, J., & Berrington, K. A. 1995, A&AS, 110, 209
Piña, R. K., & Puetter, R. C. 1993, PASP, 105, 630
Porter, L. J., & Klimchuk, J. A. 1995, ApJ, 454, 499
Pottasch, S. R. 1963, ApJ, 137, 945
———. 1964, Space Sci. Rev., 3, 816
Raymond, J. C., & Doyle, J. G. 1981, ApJ, 247, 686
Rosner, R., Golub, L., & Vaiana, G. S. 1985, ARA&A, 23, 413
Rosner, R., Tucker, W. H., & Vaiana, G. S. 1978, ApJ, 220, 643
Sampson, D. H., Goett, S. J., & Clark, R. E. H. 1984, At. Data Nucl. Data Tables, 30, 125
Sampson, D. H., Zhang, H. L., & Fontes, C. J. 1990, At. Data Nucl. Data Tables, 44, 209
Schmitt, J. H. M. M., Drake, J. J., Stern, R. A., & Haisch, B. 1996, ApJ, 457, 882
Schrijver, C. J., Mewe, R., van den Oord, G. H. J., & Kaastra, J. S. 1995, A&A, 302, 438
Serio, S., Peres, G., Vaiana, G. S., Golub, L., & Rosner, R. 1981, ApJ, 243, 288
Sheeley, N. R. 1996, ApJ, 469, 423
Siarkowski, M. 1983, Sol. Phys., 84, 131
Spadaro, D., Orlando, S., Peres, G., & Leto, P. 1995, A&A, 302, 285
Stern, R. A., Lemen, J. R., Schmitt, J. H. M. M., & Pye, J. P. 1995, ApJ, 444, L45
Storey, P. J., Mason, H. E., & Saraph, H. E. 1996, A&A, 309, 677
Sturrock, P. A., Wheatland, M. S., & Acton, L. W. 1995, ApJ, 461, L115
Sylwester, J., Schrijver, J., & Mewe, R. 1980, Sol. Phys., 67, 285
Tayal, S. S., Henry, R. J. W., & Pradhan, A. K. 1987, ApJ, 319, 951
Thomas, R. J., & Neupert, W. M. 1994, ApJS, 91, 46
Thompson, A. M. 1991, in Intensity Integral Inversion Techniques: A Study in Preparation for the SOHO Mission, ed. R. A. Harrison & A. M. Thompson, SERC Tech. Rep. RAL-91-092 (Oxfordshire, UK: Rutherford Appleton Lab.), 18
Tolstoy, E., & Saha, A. 1996, ApJ, 462, 672
Tsuneta, S. 1997, in ASP Conf. Proc., High-Resolution Solar Atmospheric Dynamics Workshop, ed. E. Deluca & J. Bookbinder (San Francisco: ASP), in press
Tsuneta, S., et al. 1991, Sol. Phys., 136, 37
Unnikrishnan, K., Callaway, J., & Oza, D. H. 1991, Phys. Rev. A, 43, 5966
Vaiana, G. S., Davis, J.M., Giacconi, R., Krieger, A. S., Solk, J. K., Timothy, A. F., & Zombeck, M. 1973, ApJ, 185, L47
Wheatland, M. S., Sturrock, P. A., & Acton, L. W. 1997, ApJ, 482, 510
Withbroe, G. L. 1975, Sol. Phys., 45, 301
Yoshida, T., Tsuneta, S., Golub, L., Strong, K., & Ogawara, Y. 1995, PASJ, 47, L15
Young, P. R., Landi, E., & Thomas, R. J. 1998, A&A, 329, 291 (Y98)
Zhang, H. L., Graziani, M., & Pradhan, A. K. 1994, A&A, 283, 319
Zhang, H. L., & Sampson, D. H. 1992, At. Data Nucl. Data Tables, 52, 143
Zhang, H. L., Sampson, D. H., & Fontes, C. J. 1990, At. Data Nucl. Data Tables, 44, 31